

NASA MEMO 12-1-58A

NASA

MEMORANDUM

ESTIMATION OF DIRECTIONAL STABILITY DERIVATIVES
AT MODERATE ANGLES AND SUPERSONIC SPEEDS

By George E. Kaattari

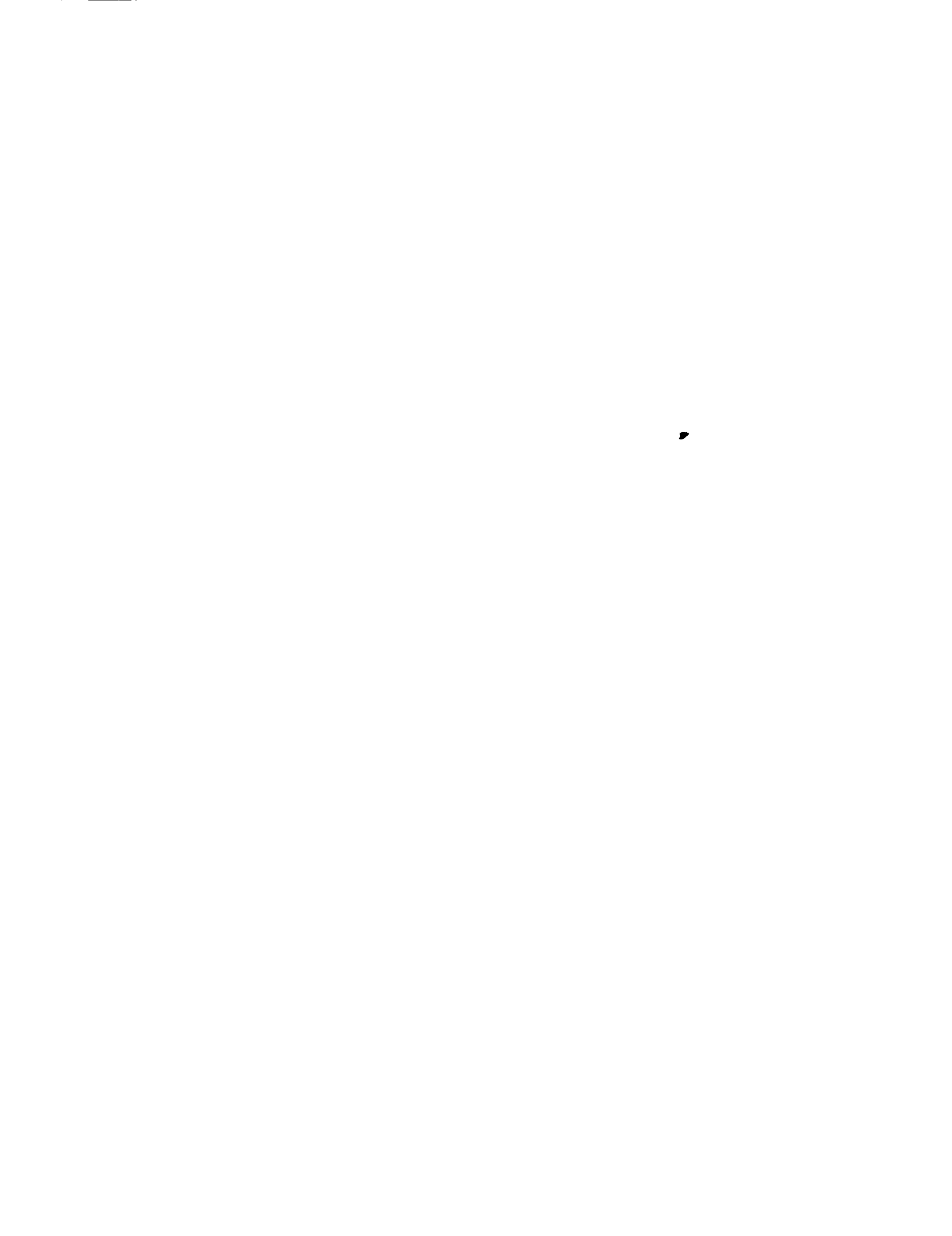
Ames Research Center
Moffett Field, Calif.

**NATIONAL AERONAUTICS AND
SPACE ADMINISTRATION**

WASHINGTON

January 1959

Declassified December 8, 1961



NATIONAL AERONAUTICS AND SPACE ADMINISTRATION

NASA MEMO 12-1-58A

ESTIMATION OF DIRECTIONAL STABILITY DERIVATIVES

AT MODERATE ANGLES AND SUPERSONIC SPEEDS

By George E. Kaattari

SUMMARY

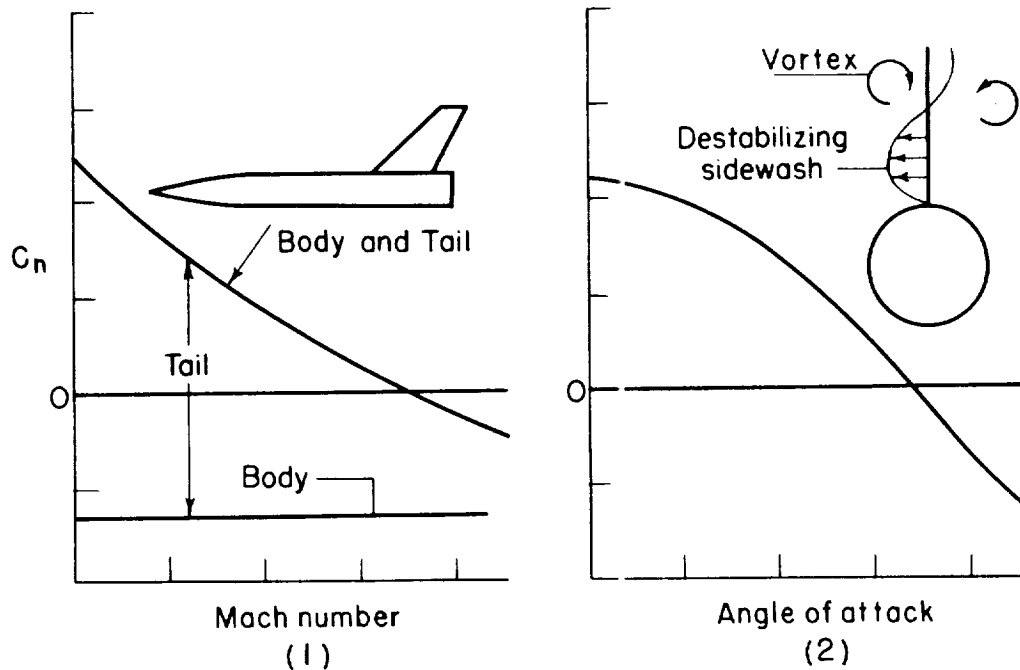
A study of some of the important aerodynamic factors affecting the directional stability of supersonic airplanes is presented. The mutual interference fields between the body, the lifting surfaces, and the stabilizing surfaces are analyzed in detail. Evaluation of these interference fields on an approximate theoretical basis leads to a method for predicting directional stability of supersonic airplanes. Body shape, wing position and plan form, vertical tail position and plan form, and ventral fins are taken into account. Estimates of the effects of these factors are in fair agreement with experiment.

INTRODUCTION

Aircraft designed for supersonic flight have problems of directional instability. The difficulty arises primarily because the center of gravity of the supersonic fuselage-engine combination is well aft of the fuselage nose. The resulting "short" afterbody then restricts the "moment arm" available to the stabilizing surfaces. Current methods of compensating for this moment arm penalty are largely limited to the use of large vertical tails and auxiliary fins, such as "strakes" or ventral fins. Destabilizing aerodynamic effects which compound the difficulty of maintaining directional stability occur with increasing angle of attack and Mach number.

The important aerodynamic factors contributing to directional instability of supersonic airplanes were briefly pointed out in reference 1. These factors are reviewed here to outline the nature of the study which will subsequently be undertaken in this report. The directional characteristics of an airplane are dominated by those of the body and the vertical tail. Insight into the directional stability characteristics of a

supersonic airplane is then provided by considering the properties of a body-tail configuration. Vertical-tail surfaces are used to compensate for the directional instability of the fuselage and to give positive directional stability to the combination. The stabilizing moment of the combination about the fuselage center of gravity can be separated into moments caused by the tail and the body alone. The unstable moment coefficient of the fuselage is nearly independent of Mach number. The stabilizing moment contributed by the tail decreases with increasing Mach number approximately as $1/\sqrt{M_\infty^2-1}$, and the directional moment coefficient of the combination then also decreases with Mach number, as shown in sketch (a1). Further decreases in the moment coefficient occur when the airplane is at combined sideslip and large angle of attack. This additional loss in stabilizing moment is caused by destabilizing elements in the fuselage sidewash wake acting on the vertical-tail panels. This wake is generally characterized by the presence of two body vortices whose strength increases approximately in proportion to the square of angle of attack. At angles of sideslip, the vortex pair is asymmetrically disposed with respect to the tail plane and causes a destabilizing sidewash with the attendant stability characteristics shown in sketch (a2). The combined



Sketch (a)

effect of Mach number and angle of attack in many instances can cause an airplane to become directionally unstable.

It is the purpose of this report to present a method for quantitatively predicting the foregoing destabilizing effects along with the less obvious aerodynamic effects of a wing on directional stability of a body and body-tail in combination.

SYMBOLS

The results are presented as standard NACA coefficients of forces and moments. The data are referred to the body axis system with the reference center of moments located as indicated in figure 1.

a	body vertical semiaxis, in.
b	body horizontal semiaxis, in.
B	body
c_{d_c}	crossflow drag coefficient
c_r	wing root chord at body juncture, in.
\bar{c}	distance to center of pressure from the juncture of wing leading edge and body, in.
C_n	yawing-moment coefficient, $\frac{\text{yawing moment}}{q_{\infty W}^2 s_W}$
C_Y	side-force coefficient, $\frac{\text{side force}}{q_{\infty W}}$
d	body diameter, in.
H	horizontal stabilizer
i_V	vortex interference coefficient
$k(\alpha)$	body-wing interference coefficient due to angle of attack
K	interference coefficient
l	body length, in.
\bar{l}	distance of center of pressure from body nose, in.
l_M	distance to moment reference point from body nose, in.
l_N	length of body ahead of juncture of the wing leading edge and body, in.

M	local Mach number
M_C	crossflow Mach number, $M_\infty \sin \sqrt{\alpha^2 + \beta^2}$
M_∞	free-stream Mach number
N	yawing moment, lb in.
p	local static pressure, lb/sq in.
p_∞	free-stream static pressure, lb/sq in.
q	local dynamic pressure, lb/sq in.
q_∞	free-stream dynamic pressure, lb/sq in.
r	body radius, in.
s_U	ventral-fin span from body axis, in.
s_V	vertical-tail span from body axis, in.
s_W	wing semispan, in.
S_B	maximum cross-sectional area of body, sq in.
S_p	projected area of body on vertical plane, sq in.
S_W	total area of wing including portion blanketed by body, sq in.
U	ventral fin
v	lateral component of free-stream velocity
V	upper vertical tail
w	vertical component of free-stream velocity
W	wing
x	body coordinate measured from nose
X	streamwise coordinate
Z	vertical coordinate
α	angle of attack, radians unless noted
β	angle of sideslip, radians unless noted

γ	ratio of specific heats, 1.40
Γ_B	body vortex strength
Δ	index denoting increment
ϵ	angle between tail leading edge and body center line, deg
η_B	corrective coefficient to body-wing interference coefficient of slender-body theory
η_W	effectiveness factor involved in wing expansion or compression fields
κ	proportionality constant
λ	taper ratio

Subscripts

B	body
H	horizontal tail
s	vortex separation
U	ventral fin
V	upper vertical tail
W	wing
BV	combination of body and upper vertical tail
BVU	combination of body, upper vertical tail, and ventral fin
BW	combination of body and wing
BWV	combination of body, wing, and upper vertical tail
BWVH	combination of body, wing, upper vertical tail, and horizontal tail
BWVU	combination of body, wing, upper vertical tail, and ventral fin
()	in presence of (e.g., B(V), body in presence of upper vertical tail)

β	coefficient derivative (e.g., $()_{\beta}$, derivative of coefficient in parentheses with respect to sideslip angle β)
φ	cross-coupling coefficient

Superscripts

+	compression field
-	expansion field
F	sweptforward wing
R	reversed wing

ANALYSIS

As a guide to development of the estimation procedures of the present report, a systematic series of tests on a variety of airplanes was required. In particular, tests were needed to reveal the directional stability increments contributed by each component in a progressive build-up from a basic body to a complete airplane. The bulk of such experimental data were provided through tests of the configurations shown in figure 1 in the Ames 1- by 3-foot supersonic wind tunnel No. 2 at Mach numbers 1.97 to 2.94. A description of this facility is given in reference 2. Additional data were taken from references 3 to 5.

The estimation procedures to be presented in the present report are an extension to those of reference 6. The linear theory is reviewed for completeness of presentation, but emphasis is given to nonlinear effects attending large angles of inclination.

To determine the aerodynamic characteristics of a body-component combination the body and component characteristics must be known independently, as well as the mutual interactions existing between the body and components in combination. The method of determining mutual interference effects at low angles is based on the result from slender-body theory that the ratio of the change in side force due to the addition of a surface to a body to the side force developed by the surface alone is in the same ratio as the change in the apparent mass (of the body-surface cross section in sideslip) due to the addition of the surface to the apparent mass of the surface alone. The change or increment in apparent mass due to the addition of a component to a pre-existing configuration causes a redistribution of force interactions among the components. The distribution of this incremental side force among the components is not

determined in the analysis to be presented; only the total change is known. This incremental side force is simply charged to the component that produces the change. As a consequence of this procedure, the order in which a configuration is constructed affects the "interference coefficients." Accordingly, the interference coefficients presented must be used in the order prescribed. Two sets of interference coefficients are presented: (1) coefficients which are applicable to uncoupled wing-tail configurations (aircraft having no interaction between the wing and directional stabilizers), and (2) coefficients applying to closely coupled wing-tail configurations (aircraft with wing in close proximity to the directional stabilizers). Symbolic designations of the incremental interference coefficients K or apparent mass ratio changes along with associated force designations are illustrated in figure 2 for coupled and uncoupled wing-tail configurations. The symbols are arranged in a sequence indicating the order of configuration build-up to be employed. Isolated component forces, denoted Y , are determined by estimate or experiment. Figures giving values for the interference coefficients K are introduced at appropriate sections in the text. The foregoing is essentially a review of the method of reference 6 for estimating the directional stability coefficients of airplanes at low angles of sideslip and attack.

In the following sections the theoretical directional stability coefficients of various body-component combinations are derived, beginning with an initial consideration of the directional characteristics of four different bodies. Methods applicable to determining the incremental directional coefficients resulting from the addition of various components are then considered at each stage of a configuration build-up. Linear theory applicable at low angles is presented for each case, followed by methods for estimating the nonlinear effects introduced by large angles of inclination. Correlation of experiment and theory at both low and high angle ranges is discussed.

Body Alone

Pure sideslip.- Available theories generally give satisfactory values for aerodynamic forces on a body. On the other hand, simple methods of estimating the center of pressure of these forces are unavailable. In view of the lack of accurate theory for determining body centers of pressure, estimates of body-alone yawing moments are omitted in the present report. Consideration, however, is given to determining side force of bodies for the sake of maximum completeness of presentation. The value of the side-force coefficient near $\beta = 0^\circ$ for circular bodies is given by slender-body theory as

$$C_{Y_B} = 2\beta \quad (1a)$$

based on maximum body cross-sectional area. At large angles of sideslip, force coefficients of bodies become nonlinear with angle of inclination as a result of the effects of viscous separation and are then grossly underestimated by slender-body theory. The nonlinear increase in the force coefficient can be empirically taken into account, by the method of reference 7, through an additive body crossflow coefficient term

$$c_{d_c} \frac{S_P}{S_B} \beta^2 \quad (1b)$$

where c_{d_c} is the two-dimensional drag coefficient for the body cross section and S_P is the projected body area normal to the crossflow direction. It is assumed that, at supersonic speeds, the crossflow about the body at a given longitudinal location is unaffected by "end effects" of body nose or base. The use of two-dimensional crossflow coefficients is then possible. An investigation of bodies having elliptical cross sections (refs. 2 and 8) shows that the experimental side-force coefficient slopes are predicted with fair accuracy when equation (1a) is modified by the ratio of the semiaxes lengths, a/b , in accordance with slender-body theory. The investigation shows further that the force coefficients of an elliptical and circular body of the same base reference area are in the ratio a/b over a wide range of sideslip angles. Thus, the term a/b affects the potential (linear) and viscous (nonlinear) terms of body force coefficients in the same degree. In most cases bodies are either nearly circular or elliptical in cross section. An approximate method of determining the side-force coefficient for these cases is based on two assumptions: (1) The linear term is given by slender-body theory and is

$$C_{Y_B} = \frac{a}{b} 2\beta \quad (2a)$$

where a/b pertains to the semiaxis ratio at the maximum cross-sectional area, S_B , location. (2) Essentially two-dimensional crossflow prevails at each section and the local crossflow coefficient is given, by generalizing the results of reference 8, as the local semiaxes ratio a/b as a function of x times the crossflow coefficient of a circular cross section. The nonlinear crossflow force is then the integrated effect of local crossflow coefficients over the projected body area. Within the limitation of these assumptions the total side-force coefficient is

$$C_{Y_B} = \frac{a}{b} \frac{S_B}{S_W} 2\beta + \left[\frac{2c_{d_c}}{S_W} \int_0^l \frac{a}{b} (x) a(x) dx \right] \beta^2 \quad (2b)$$

Equation (2b) gives side-force coefficients that are in fair accord with experimental values, as will be shown.

Combined angles of attack and sideslip.- An expression giving the side-force coefficients for a circular cross-section body ($a/b = 1$) in combined sideslip and angle of attack is given simply as the sideslip (β) component of the force coefficient associated with the total angle of inclination ($\alpha' = \sqrt{\alpha^2 + \beta^2}$); that is,

$$\begin{aligned} C_Y &= \frac{S_B}{S_W} 2\alpha' \left(\frac{\beta}{\alpha'} \right) + c_{d_c} \frac{S_P}{S_W} \alpha'^2 \left(\frac{\beta}{\alpha'} \right) \\ &= \frac{S_B}{S_W} 2\beta + c_{d_c} \frac{S_P}{S_W} \beta \sqrt{\alpha^2 + \beta^2} \end{aligned} \quad (3)$$

For bodies of noncircular cross section ($a/b \neq 1$), the force vector does not necessarily lie in the plane of maximum body inclination α' . This fact precludes simple estimates of side-force coefficients of other than circular cross-section bodies at combined pitch and sideslip angles.¹

Comparison of estimate and experiment.- In order to evaluate the side-force coefficients of bodies, the crossflow drag coefficient for circular bodies must be known. At low, subsonic crossflow velocities, the drag coefficient c_{d_c} is 1.2. At high velocities ($M_c > 0.4$), c_{d_c} varies significantly and the variation must be taken into account. Experimental values for c_{d_c} at the Reynolds number of the present test were abstracted from reference 10 and are plotted as a function of crossflow Mach number, M_c , in figure 3. These estimates for c_{d_c} were used in evaluating equations (2b) and (3). Figure 4 is a plot of experimental and estimated values of C_Y as a function of sideslip angle β for three body models of the present test at $M_\infty = 2.94$. Good correlation between experiment and estimate is shown over the angle range investigated. It can be concluded that, for the range of body shapes investigated, equation (2b) adequately predicts the effect of "shape" on body side-force coefficients.

In figure 5 experimental and estimated values for the side-force coefficients of circular body models are plotted as a function of angle of attack for two sideslip angles. The estimated values are given by equation (3). The effect of angle of attack on the side-force coefficient is fairly well predicted. A point of particular interest lies in the fact that the effect of increased body length on the side-force coefficient (the difference of C_Y between bodies B_1 and B_{1L} at $\beta = 5^\circ$) is correctly predicted. This prediction of side-force change due to body-length change has an important bearing on the determination of the effects of body-wing interaction and will be discussed in a later section.

¹Consideration of other than circular cross-section bodies is given in reference 9.

Body-Tail Configuration

In the present method, it is assumed that the yawing-moment coefficients of the body alone have been experimentally determined. These coefficients are used in calculating values for the directional coefficients of the body in combination with wings and stabilizing surfaces.

Body-tail configuration in pure sideslip.- The total side force of the combination of a body with a tail is the sum of the forces contributed by the body alone and by the tail in presence of the body. This sum is expressed in figure 2 for a body, B, and upper vertical tail, V, as

$$Y_{BV} = Y_B + K_{V(B)} Y_V \quad (4a)$$

It is convenient, in comparisons with experiment, to express equations for the directional coefficients in a form which denotes the stabilizing contribution of the added component. Accordingly, equation (4a), expressed in coefficient form as the contribution of the tail in the presence of the body, is written

$$C_{Y_{BV}} - C_{Y_B} = K_{V(B)} C_{Y_V} \quad (4b)$$

The side-force coefficient C_{Y_V} is that of the upper tail panel when mounted on an infinite reflection plane (equivalent to one-half the coefficient of two such panels joined together). The side-force coefficient C_{Y_B} is that of the body alone. Values of $K_{V(B)}$ abstracted from reference 6 are indicated by the solid curve in figure 6 as a function of ratio of body radius to tail span.

The K coefficients take into account mutual interaction between components; for example, $K_{V(B)}$ includes the effect of interference on V due to B and the effect of force carryover onto B due to V . This is expressed symbolically as $K_{V(B)} = K_{V+B \rightarrow V} + K_{V \rightarrow B}$. A breakdown of these interference effects is not essential in determining total side force; however, the division of loading between body and tail and the corresponding centers of pressure (\bar{l}) must be known in order to determine yawing moment accurately. Since the present method does not give a division of the interference forces, an approximate method of determining moment values is employed. This method is developed as follows:

$$N_{BV} = N_B + N_{V+B \rightarrow V} + N_{V \rightarrow B}$$

or

$$N_{BV} = N_B + (\bar{l}_V - l_M) \left(\frac{\bar{l}_{V+B \rightarrow V} - l_M}{\bar{l}_V - l_M} Y_{V+B \rightarrow V} + \frac{\bar{l}_{V \rightarrow B} - l_M}{\bar{l}_V - l_M} Y_{V \rightarrow B} \right) \quad (5a)$$

The distance to the tail center of pressure from the moment reference point ($\bar{l}_V - l_M$) in the absence of body interference is introduced in equation (5a). This value is not significantly different from that of the tail in the presence of the body ($\bar{l}_{V+B \rightarrow V} - l_M$). It is assumed that the center-of-pressure location of the force distribution on the body due to the tail ($\bar{l}_{V \rightarrow B}$) is approximately that of the isolated tail. Within these approximations, and with $Y_{V(B)} = Y_{V+B \rightarrow V} + Y_{V \rightarrow B} = K_{V(B)} Y_V$, equation (5a) can be simplified and written in coefficient form as the yawing-moment contribution of a tail in the presence of a body

$$C_{n_{BV}} - C_{n_B} = \frac{\bar{l}_V - l_M}{2s_W} K_{V(B)} C_{Y_V} \quad (5b)$$

The side-force-coefficient increment due to a tail assembly including a ventral fin is

$$C_{Y_{BVU}} - C_{Y_B} = K_{V(B)} C_{Y_V} + K_{U(BV)} C_{Y_U} \quad (6)$$

Values for $K_{U(BV)}$ are also given in figure 6 by the dashed line parameters which take into account the effect of the upper tail. The definition of C_{Y_U} is similar to that of C_{Y_V} . The incremental yawing-moment-coefficient equation is developed through steps similar to those leading to equation (5b) to be

$$C_{n_{BVU}} - C_{n_B} = \left(\frac{\bar{l}_V - l_M}{2s_W} \right) K_{V(B)} C_{Y_V} + \left(\frac{\bar{l}_U - l_M}{2s_W} \right) K_{U(BV)} C_{Y_U} \quad (7)$$

Body-tail in combined sideslip and angle of attack. - The effects of angle of attack on the directional coefficients of body-tail configurations, and of configurations in general, arise from two distinct aerodynamic interference phenomena. These are (1) a cross-coupling effect of sideslip and angle of attack induced crossflow velocities, discussed in reference 11, and (2) an induced sidewash due to vortices (particularly those forming about the body at high angles of attack). These two effects are discussed in turn.

The cross-coupling interference phenomenon is taken into account by the factor K_ϕ , developed in reference 11, with which the modifying effect of angle of attack on the tail contribution to the side-force coefficient of a body-tail combination can be determined. The increment in side-force coefficient is given by the equation

$$C_{Y_V(\beta, \alpha)} = -K_\phi \frac{\alpha}{\tan \epsilon_V} C_{Y_V} \quad (8)$$

The factor K_{ϕ} is plotted as a function of ratio of panel semispan to body radius, r/s_V , in figure 7 for a planar and a cruciform body-tail configuration. It is to be noted that values are given only for equispan double and cruciform panel body configurations. Solutions for a single panel and body combination are not available at present. However, the experimental results of reference 11 show that panel-to-panel effects are negligible for a planar configuration with $r/s_V = 0.273$ and $M_{\infty} = 2$. It is then indicated that for Mach numbers of 2 or greater, the K_{ϕ} applying to planar (two surface) configurations can also be applied to a single surface configuration. In most cases considered in this report the Mach number is 2 or greater and the values presented in figure 7 are adopted.

In order to estimate the effects of body-vortex induced sidewash on the tail side-force coefficient, the position of the vortices with respect to the tail plane and the strength of the vortices must be known. Theoretical methods for determining the position and strength of body vortices involve very laborious calculations even for circular bodies and are unavailable for noncircular bodies. An experimental correlation of these quantities is presented in reference 12 for circular bodies and provides a simple estimate for vortex strengths and positions in lieu of theory. With these quantities in hand, the effect of body vortices on the upper tail side force is related to the tail-alone side force developed at the angle of inclination $\alpha' = \sqrt{\alpha^2 + \beta^2}$ by the factor Δi_V and the body vortex strength Γ_B

$$C_{Y_V(\Gamma_B)} = \Delta i_V \frac{\Gamma_B}{2\pi\sqrt{v^2+w^2} r \left(\frac{s_V}{r} - 1\right)} C_{Y_V(\alpha')} \quad (9)$$

Values for Δi_V are determined, as shown by the example in the appendix, from figure 8. Interference factors (i_V) for this chart were determined by the equations of reference 13 for the effect of a single external vortex and its body image on an upper tail panel. (The effect of two external vortices is found by superposition.) This chart applies strictly to a tail panel of taper ratio $\lambda = 1/2$ and $r/s_V = 0.2$ corresponding approximately to that of model B₁V₅. The use of this chart for panels of other taper ratios will be discussed in a following section on experimental considerations.

The side-force coefficient contribution of an upper tail to a body-tail combination at combined sideslip and angle of attack is then given by the sum of equations (4), (8), and (9)

$$C_{Y_{BV}} - C_{Y_B} = \left(K_V(B) - \frac{K_{\phi}\alpha}{\tan \epsilon_V} \right) C_{Y_V} + C_{Y_V(\Gamma_B)} \quad (10)$$

The yawing-moment coefficient is

$$C_{n_{BV}} - C_{n_B} = \left(\frac{\bar{l}_V - l_M}{2s_W} \right) \left[\left(K_{V(B)} - \frac{K_{\phi\alpha}}{\tan \epsilon_V} \right) C_{Y_V} + C_{Y_V(\Gamma_B)} \right] \quad (11)$$

The directional coefficients for a body-tail configuration including a ventral fin are obtained in a similar manner but with the cross-coupling term additive.

$$C_{Y_{BVU}} - C_{Y_B} = \left[K_{V(B)} - \frac{K_{\phi\alpha}}{\tan \epsilon_V} \right] C_{Y_V} + \left[K_{U(BV)} + \frac{K_{\phi\alpha}}{\tan \epsilon_U} \right] C_{Y_U} + C_{Y_V(\Gamma_B)} + C_{Y_U(\Gamma_B)} \quad (12)$$

and

$$C_{n_{BVU}} - C_{n_B} = \left(\frac{\bar{l}_V - l_M}{2s_W} \right) \left[\left(K_{V(B)} - \frac{K_{\phi\alpha}}{\tan \epsilon_V} \right) C_{Y_V} + C_{Y_V(\Gamma_B)} \right] + \left(\frac{\bar{l}_U - l_M}{2s_W} \right) \left[\left(K_{U(BV)} + \frac{K_{\phi\alpha}}{\tan \epsilon_U} \right) C_{Y_U} + C_{Y_U(\Gamma_B)} \right] \quad (13)$$

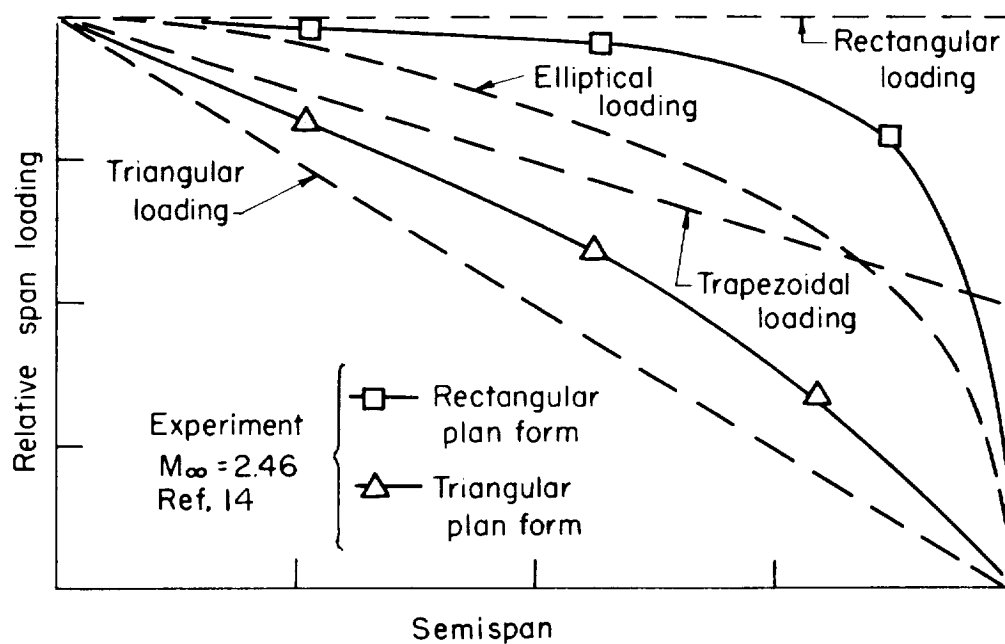
Comparison of estimate and experiment.- Estimated and experimental directional coefficients of body-tail combinations are compared on the basis of the coefficient values of the body and tail in combination minus that of the body alone. These comparisons are presented in figure 9. Discussion is expedited by being directed primarily to the correlation between experimental and estimated directed side-force coefficients because the degree of correlation of yawing-moment data with estimates closely parallels that of the side force.

The estimated values given apply strictly to the circular body-tail model B₁V₅ (fig. 9(a)). It is evident from the data that a strong destabilizing effect occurs with increasing angle of attack. The estimated side-force coefficient, given by equation (4), is applicable at $\alpha = 0^\circ$ (pure sideslip) and is in good accord with experimental values. If cross coupling is taken into account in the method (eqs. (4) and (8)), an appreciable decrease in the directional coefficients results which, however, accounts only partially for the experimental decrease. Finally, equation (10), which takes into account both cross coupling and body-vortex effects, is in good accord with experimental values over the angle-of-attack range of the test. Most of the remaining correlation figures, 9(b) to (f), show good agreement of estimate with experiment. It should be noted that figures 9(e) and (f) give the incremental coefficients in derivative form at $\beta \approx 0^\circ$.

The effect of body shape on the tail contribution to directional coefficients of body-tail combinations cannot be predicted quantitatively since the theoretical effects of body shape on vorticity and cross coupling are unknown. Accordingly, the effects of body shape were evaluated experimentally. To this end, coefficients for all three basic models are plotted in figure 9(a) to facilitate comparison. At the sideslip angle $\beta = 5.1^\circ$, the coefficients of the tail in presence of both the elliptic body B_2 and the double elliptic body B_3 are less affected by angle of attack than in the presence of the circular body B_1 . At sideslip angle $\beta = 10^\circ$, there is less effect of body shape among these models.

A comparison of the side-force contribution of a tail on the extended nose circular model B_{1L} with that of the same tail (V_2) on a rectangular afterbody model B_A (fig. 9(c)) indicates large influence of body shape. The rectangular model is considerably less stable over the angle-of-attack range than is the extended-nose model. A direct comparison of the effect of the two bodies on directional coefficients is not strictly justified since B_A has somewhat greater volume than B_{1L} and the strength of its vortex wake may be expected to be the larger. More important with regard to tail "effectiveness" are the different distributions of vorticity brought about by the difference in body shape of the two bodies. Vapor-screen pictures revealing this vorticity about bodies B_A and B_{1L} in the vicinity of the tail surface are shown in figure 10. Body B_A has three distinct regions of vorticity, the strongest lying in close proximity to the plane of the vertical tail. Body B_{1L} has two equal-strength vortices, one of which again lies in close proximity to the tail plane. The degree of destabilizing effect of body vortices on the vertical-tail surface is dependent on the vortex positions with respect to one another and on their relative position with respect to the tail plane. Vortices of equal strength (with opposite rotation) in close proximity to each other relative to their mean distance from the tail surface induce small destabilizing sidewash. Vortices in close proximity to the body have less effect than when outboard. (The foregoing statements are readily verified by inspection of i_y values in fig. 8.) Examination of the vapor-screen photographs in figure 10 show that in the case of body B_A the vortices are more widely separated from one another than are those about body B_{1L} . Furthermore, the dominant (and destabilizing) vortex at the plane of the tail is at a greater tail spanwise distance from the body B_A than is the destabilizing vortex of body B_{1L} . These differences in position are the probable cause for the relatively poor stability characteristics of $B_A V_2$ in comparison with those of $B_{1L} V_2$. It is to be noted that the cross-sectional shape of the afterbody of B_A (fig. 1(a)) has relatively sharp corners. A plausible illustration of how these "corners" can promote the formation of vorticity into the complex wake is shown in figure 10. In effect, corner vortices generated at sideslip and at angle of attack are swept in the direction of resultant flow to form the asymmetrical pattern shown. In view of this, deep angular body cross-sectional shapes may be undesirable since they can augment the unfavorable disposition of body vorticity about the tail.

In determining the effects of vortex-induced sidewash on tail effectiveness, no account was taken of tail plan form as a variable. As stated previously, the influence of body vortices on a tail plan form corresponding to that of V_5 was used as a basis for the chart of figure 8. The general, though approximate, applicability of the chart for all plan forms (with $r/s_y \approx 0.2$) is justified by experimental considerations. As in reference 13, it is assumed that the loss in tail loading at a given span location is proportional to the product of local chord length and the local change in flow inclination due to vortex-induced crossflow. The total tail-load loss is then determined by "strip" integration of this loading loss over the exposed tail span. It is assumed in this procedure that a constant flow inclination with respect to the tail surface produces a span load distribution proportional to chord length distribution. In actuality, plan forms at moderate Mach numbers and low angles of inclination tend to develop a loading intermediate between elliptical and plan formlike in spanwise distribution. This tendency is illustrated in sketch (b) in which comparison is made between



Sketch (b)

elliptical loading and normalized experimental loading for surfaces of rectangular and triangular plan form. It is evident that the assumption of plan formlike distribution of loading for each surface is not essentially any more valid than assigning an elliptical loading to both surfaces. Since the actual loading does not correspond to either type, a straight-line (trapezoidal) loading was adopted as a reasonable compromise for the sake of computational simplicity. This trapezoidal loading was

used to determine the values presented in the chart of figure 8. This loading corresponds to the span distribution of chord length for the V_5 tail plan form.

The foregoing concession made to computational simplicity is experimentally justified since the degree of correlation between experiment and theory does not vary significantly among the trapezoidal (fig. 9(a)), triangular (fig. 9(b)), and near rectangular (fig. 9(d)) plan-form tails investigated. In the case of the clipped tail (fig. 9(d)), additional computations using the equations of reference 13 were required since body radius to span ratio was considerably larger than 0.2, precluding the use of figure 8. It is evident in figure 9(d) that the ratio of stabilizer effectiveness at high angle of attack to its value of $\alpha = 0^\circ$ is substantially reduced for the short or clipped span tail V_6C in comparison to that of the unclipped tail V_6 . This is because a short span tail has a large portion of its surface exposed to the region of adverse sidewash existing between the destabilizing vortex core and the body surface.

Additional correlation of estimated values with experiment is presented in figures 9(e) and 9(f) for directional coefficient derivatives with $\beta \approx 0^\circ$ of two configurations, one of which includes a ventral fin, at Mach numbers of 1.41 and 2.0. Poor absolute value correlation exists at $M = 1.41$, although the qualitative effect of angle of attack is well predicted. Improved correlation in this case would undoubtedly result if the experimental value for the tail-alone side-force coefficient were known and substituted in place of the estimated value in equations (12) and (13).

Body-Wing Combination

Wing-body interaction does not occur in pure sideslip in the case where the wing position coincides with the body horizontal plane of symmetry other than for small effects of wing thickness. This is true since the wing plane then coincides with a body-alone crossflow streamline and no change in crossflow takes place. At combined angles and particularly for the case where the wing is in an extreme, or tangent, location on a circular or nearly circular body, interference forces develop which can have significant effects on the directional coefficients of airplanes.

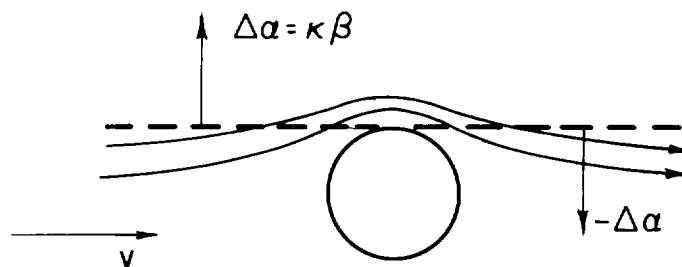
Body-wing in pure sideslip. - The following expression from slender-body theory accounts for the increase in body side force due to the addition of a tangent wing to the body:

$$C_{Y_{B(W)}} = K_{B(W)} \frac{S_B}{S_W} 2\beta \quad (14)$$

The factor $K_{B(W)}$ denotes the ratio of increase in side-force coefficient referred to body area reference S_B and is plotted as a function of the ratio of wing semispan to body radius, r/s_W , in figure 11. The term 2β is the usual slender-body-theory force coefficient for a circular body.

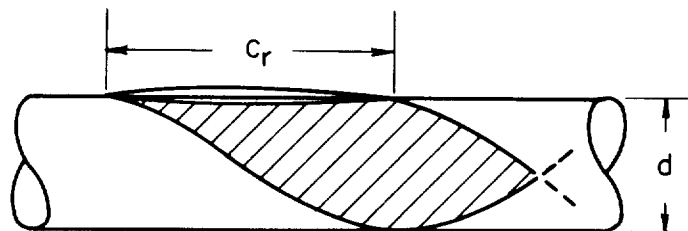
It was shown in reference 6 that, in general, interference coefficients derived from slender-body theory can be applied with acceptable accuracy to nonslender configurations and to configurations at supersonic Mach numbers. In most cases the effect of Mach number is automatically taken into account by the side-force coefficient of the reference components to which each interference coefficient applies. Equation (14) does not take into account the effect of Mach number since here the reference component side-force coefficient involved (2β) is that of the body alone which depends only on sideslip angle. A method is sought by which Mach number effects can be taken into account by a modification to equation (14) (strictly valid only for slender bodies at $M = 1$).

Because of the influence of the forebody on crossflow, the two wing panels effectively encounter opposing angles of attack, as indicated in the following sketch of a high wing-body configuration.



Sketch (c)

These effective angles of attack are proportional to sideslip angle $\kappa\beta$ and cause a lift on the windward panel and a download on the leeward panel. These loads create interference pressures on the body. Wing influence on the body is assumed to be confined between Mach helices originating on the leading and trailing edges of the junctures of the wing root and body, as indicated by the shaded area in sketch (d).



Sketch (d)

It is assumed that the differential pressures acting on the body are proportional to those between the wing panels and are given approximately in coefficient form by two-dimensional theory as:

$$\frac{\Delta p}{q_\infty} = \frac{2\Delta\alpha}{\sqrt{M_\infty^2-1}} - \frac{-2\Delta\alpha}{\sqrt{M_\infty^2-1}} = \frac{4\kappa\beta}{\sqrt{M_\infty^2-1}} \quad (15)$$

where κ is an undetermined proportionality factor and is assumed a constant. This pressure coefficient multiplied by the vertical area projection of the interference (shaded) area results in a value proportional to interference side force. The value of the projected area is given in terms of Mach number, body diameter, and wing root chord length by

$$\text{Area} = c_r d \left(\frac{1}{2} + \frac{\sqrt{M_\infty^2-1} d}{2c_r} \sin \frac{c_r}{\sqrt{M_\infty^2-1} d} \right) \quad \text{for } c_r < \sqrt{M_\infty^2-1} \pi d \quad (16a)$$

or

$$= \sqrt{M_\infty^2-1} \pi d^2 / 2 \quad \text{for } c_r > \sqrt{M_\infty^2-1} \pi d \quad (16b)$$

Multiplying equation (15) by equation (16a) or (16b) results in a measure of the interference force:

$$Y_{B(W)} \sim \frac{4c_r d}{\sqrt{M_\infty^2-1}} \left(\frac{1}{2} + \frac{\sqrt{M_\infty^2-1} d}{2c_r} \sin \frac{c_r}{\sqrt{M_\infty^2-1} d} \right) \kappa \beta \quad \text{for } c_r < \sqrt{M_\infty^2-1} \pi d \quad (17a)$$

or

$$2\pi d^2 \kappa \beta \quad \text{for } c_r > \sqrt{M_\infty^2-1} \pi d \quad (17b)$$

It is noted that for $c_r > \sqrt{M_\infty^2-1} \pi d$, the interference force (eq. (17b)) becomes independent of Mach number and reduces to dependence only on body diameter. Division of equation (17b) by (17a) results in the ratio, η_B , a measure of the effect of Mach number on the interference force. This ratio times the value of $K_{B(W)}$ given by slender-body theory (valid at $M_\infty = 1$) then results in the value of $K_{B(W)}$ at $M_\infty > 1$.

$$\eta_B = \frac{\pi(\sqrt{M_\infty^2-1} d/c_r)}{1+(\sqrt{M_\infty^2-1} d/c_r)\sin(c_r/\sqrt{M_\infty^2-1} d)} \quad \text{for } c_r < \sqrt{M_\infty^2-1} \pi d \quad (18a)$$

and

$$\eta_B = 1 \quad \text{for } c_r > \sqrt{M_\infty^2 - 1} \pi d \quad (18b)$$

The value of η_B is plotted as a function of $(\sqrt{M_\infty^2 - 1} d)/c_r$ in figure 12. The effect of Mach number on the interference coefficient $K_{B(W)}$ given by slender-body theory is thus determined. The side-force coefficient increment resulting from addition of a wing to a body becomes

$$C_{Y_{BW}} - C_{Y_B} = \eta_B K_{B(W)} \frac{S_B}{S_W} 2\beta \quad (19)$$

In order to determine the yawing moment contributed by the interference force, its center of pressure must be known. It is assumed that the interference pressures are uniform over the shaded area shown in sketch (d). Thus, the centroid of area is identical to the center of pressure of the interference force. The longitudinal distance to this point from the body nose is

$$\bar{l}_{B(W)} = l_N + c_r \left\{ \frac{1}{2} + \frac{\pi \left(\sqrt{M_\infty^2 - 1} d / c_r \right)^2 \sin \left(c_r / \sqrt{M_\infty^2 - 1} d \right)}{2 \left[1 + \left(\sqrt{M_\infty^2 - 1} d / c_r \right) \sin \left(c_r / \sqrt{M_\infty^2 - 1} d \right) \right]} \right\}$$

for $c_r < \sqrt{M_\infty^2 - 1} \pi d$ (20a)

and

$$\bar{l}_{B(W)} = l_N + c_r \left\{ \frac{\sqrt{M_\infty^2 - 1} \pi d}{2 c_r} \right\} \quad \text{for } c_r > \sqrt{M_\infty^2 - 1} \pi d \quad (20b)$$

The braced terms in these equations give the value of \bar{c}/c_r or the distance to the center of pressure from the juncture of the wing leading edge and root chord in terms of root-chord length, c_r . These values are presented in figure 13 as a function of $(\sqrt{M_\infty^2 - 1} d)/c_r$. The center-of-pressure position being given, the yawing-moment coefficient increment can be computed:

$$C_{n_{BW}} - C_{n_B} = \left(\frac{\bar{l}_{B(W)} - l_M}{2s_W} \right) \eta_B K_{B(W)} \frac{S_B}{S_W} 2\beta \quad (21)$$

Body-wing in combined sideslip and angle of attack.- It was pointed out that two distinct effects of angle of attack on the directional coefficients of body-tail configurations occur: the cross-coupling of upwash and sidewash velocities, and the nonlinear effect of body vortices. Higher

order slender-body solutions which account for body-wing cross-coupling are unavailable at present. However, an approximate method is developed with which the effects of angle of attack on body-wing interference coefficients can be taken into account at supersonic Mach numbers. The effect of body vortices on body-wing interference is assumed unimportant.

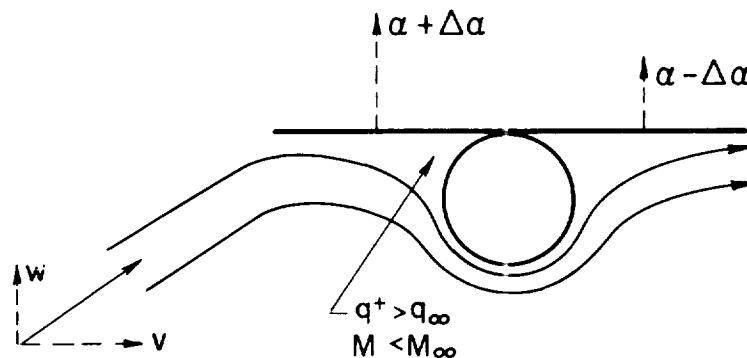
Consideration will first be given to the midbody wing location. As stated previously, the interference coefficient for such combinations is negligible in pure sideslip. An important effect arises, however, when large combined angles of attack and sideslip are imposed. This occurs since viscous crossflow, occurring at large angles of attack, is inhibited along a body length equal to the wing root chord. Thus the viscous or nonlinear forces acting on the body are reduced. Rough estimates of the amount by which the addition of a wing reduces the coefficients contributed by the body are

$$C_{Y_{BW}} - C_{Y_B} = c_{dc} \frac{c_{rd}}{S_W} \left(\beta^2 - \beta \sqrt{\alpha^2 + \beta^2} \right) \quad (22)$$

$$C_{n_{BW}} - C_{n_B} = \frac{\bar{l}_{B(W)} - l_M}{2s_W} c_{dc} \frac{c_{rd}}{S_W} \left(\beta^2 - \beta \sqrt{\alpha^2 + \beta^2} \right) \quad (23)$$

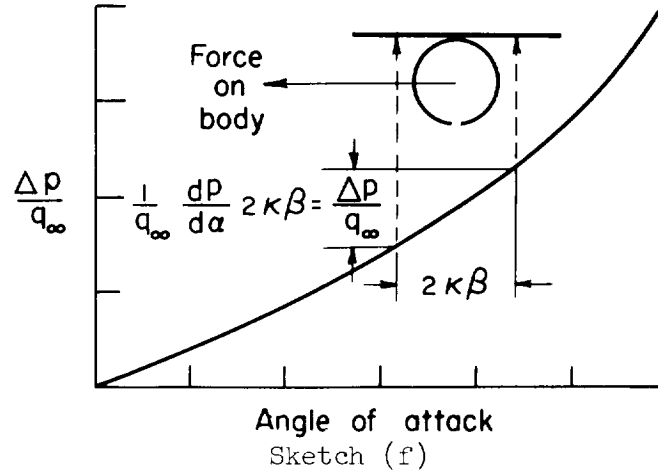
The value for $\bar{l}_{B(W)}$ depends on wing location and for mid-wing configurations can be approximated as $l_N + (1/2)c_r$.

Consideration will now be given to the effect of large angle inclination on tangent wing locations. The hypotheses are applied to a body with a high wing; however, their application to a body with a low wing is obvious. Because of the effect of the forebody on crossflow previously discussed, the wing panels are at different angles of attack. In addition, the section of the body separating the wing panels is exposed to an environment of increased dynamic pressure and reduced Mach number prevailing on the compression surface of the lifting wing. These effects are represented in sketch (e). The change in effective angle of attack



Sketch (e)

of the panels due to crossflow, $\Delta\alpha$, is again proportional to sideslip, or is $\kappa\beta$. It is now assumed that the static-pressure field, p , generated by each wing panel in the vicinity of the body is given by two-dimensional shock-expansion theory for a flat plate at angle of attack α . This pressure varies nonlinearly with angle of attack. A pressure difference exists between the wing panels since they are at different effective angles of attack as indicated in sketch (f).



This pressure differential may be determined from the derivative of p/p_∞ with α along with supersonic flow relationships between M_∞ , q_∞ , and p_∞ as given in reference 15. The differential pressure in coefficient form is separated into a linear plus a nonlinear (in square brackets) term times the differential angle $2\kappa\beta$.

$$\frac{\Delta p}{q_\infty} \sim \frac{1}{q_\infty} \frac{dp}{d\alpha} 2\kappa\beta = \left\{ \frac{2}{\sqrt{M_\infty^2 - 1}} + \frac{2}{M_\infty^2} \left[\frac{d(p/p_\infty)}{d\alpha} - \frac{\gamma M_\infty^2}{\sqrt{M_\infty^2 - 1}} \right] \right\} 2\kappa\beta \quad (24)$$

It is to be noted that equation (24) differs from equation (15) by this additional nonlinear term. The resultant reaction force on the body is proportional to this differential wing pressure times the combined effects of local dynamic pressure and Mach number, or $q\sqrt{M_\infty^2 - 1}/q_\infty\sqrt{M^2 - 1} = \eta_w$, acting on the area of the interference zone as given by equation (16) with M replacing M_∞ . The following expression can then be written for the side-force interference coefficient

$$C_{YB(W)} \sim \frac{c_r d}{q_\infty S_W} \left[\frac{1}{2} + \frac{\sqrt{M^2 - 1}}{2c_r} \sin \left(\frac{c_r}{\sqrt{M^2 - 1} d} \right) \right] \eta_w \left\{ \frac{2}{\sqrt{M_\infty^2 - 1}} + \frac{2}{\gamma M_\infty^2} \left[\frac{d(p/p_\infty)}{d\alpha} - \frac{\gamma M_\infty^2}{\sqrt{M_\infty^2 - 1}} \right] \right\} 2\kappa\beta \quad (25)$$

When $\alpha = 0^\circ$, $M = M_\infty$, $q = q_\infty$, and $\frac{d(p/p_\infty)}{d\alpha} = \frac{\gamma M_\infty^2}{\sqrt{M_\infty^2 - 1}}$ equation (25) reduces to equation (17a) in coefficient form

$$C_{Y_{B(W)}} \sim \frac{4}{\sqrt{M_\infty^2 - 1}} \frac{c_r d}{S_W} \left[\frac{1}{2} + \frac{\sqrt{M_\infty^2 - 1} d}{2c_r} \sin \left(\frac{c_r}{\sqrt{M_\infty^2 - 1} d} \right) \right] \kappa \beta \quad (26)$$

Dividing equation (25) by equation (26) gives a factor $k(\alpha)$ which takes into account the effect of angle of attack on wing-body interference.

$$k(\alpha) = \frac{\left[1 + \frac{\sqrt{M^2 - 1} d}{c_r} \sin \left(\frac{c_r}{\sqrt{M^2 - 1} d} \right) \right]}{\left[1 + \frac{\sqrt{M_\infty^2 - 1} d}{c_r} \sin \left(\frac{c_r}{\sqrt{M_\infty^2 - 1} d} \right) \right]} \left\{ 1 + \frac{\sqrt{M_\infty^2 - 1}}{\gamma M_\infty^2} \left[\frac{d(p/p_\infty)}{d\alpha} - \frac{\gamma M_\infty^2}{\sqrt{M_\infty^2 - 1}} \right] \right\} \eta_W \quad (27)$$

The ratio $k(\alpha)$ is plotted against angle of attack for various values of d/c_r and M_∞ in figure 14. Taking into account the foregoing effects of angle of attack and Mach number, the following general expressions result for the incremental coefficients.

$$C_{Y_{BW}} - C_{Y_B} = 2\eta_B K_{B(W)} k(\alpha) \frac{S_B}{S_W} \beta - \frac{c_{d_c} c_r d}{S_W} \left[\beta^2 - \beta(\alpha^2 + \beta^2)^{1/2} \right] \quad (28)$$

$$C_{n_{BW}} - C_{n_B} = \frac{\bar{l}_{B(W)} - l_M}{2s_W} \left\{ 2\eta_B K_{B(W)} k(\alpha) \frac{S_B}{S_W} \beta - \frac{c_{d_c} c_r d}{S_W} \left[\beta^2 - \beta(\alpha^2 + \beta^2)^{1/2} \right] \right\} \quad (29)$$

Values for $\bar{l}_{B(W)}$ are determined with the aid of figure 15 which gives the center-of-pressure location of the interference pressures of tangent wing-body combinations in terms of deviation from the value $\bar{c}_{(\alpha=0)}$ for the pure sideslip case given in figure 13. It is assumed that both the pressure and viscous force components of interference act at the same location.

Comparison of estimate and experiment. - Estimated and experimental side-force and yawing-moment coefficients of body-wing combinations are compared on the basis of the coefficient of the body and wing in combination minus that of the body alone. These comparisons are presented in figure 16 for side-force and in figure 17 for yawing-moment coefficients. This division between force and moment correlation presentation is made since in this case good force correlation does not generally result in

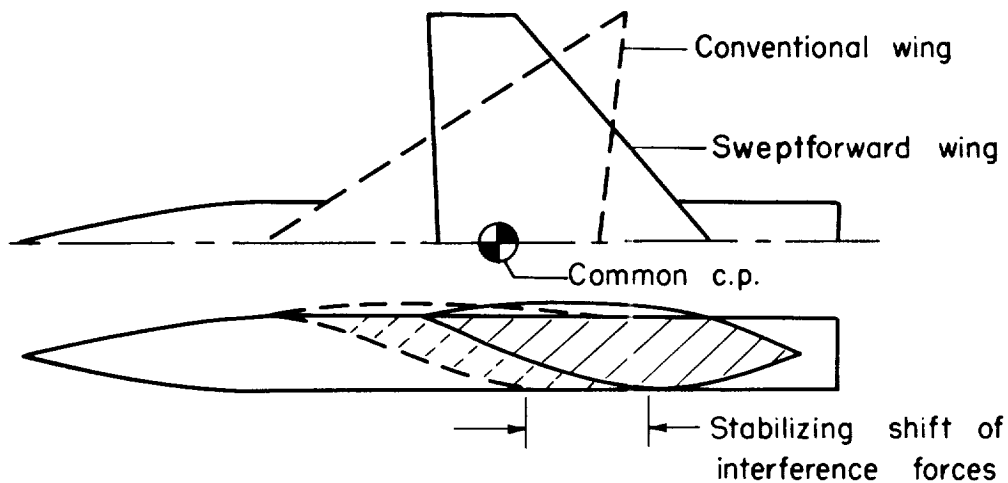
good moment correlation. This point will be discussed later in conjunction with a possible method of increasing the directional stability contribution of wing-body interference.

The experimental and theoretical values for the incremental side-force coefficient which result from the addition of a wing in a midbody location is presented in figure 16(a). Estimated values are given by equation (22) on the premise that the sole effect of the wing is to inhibit the nonlinear effects of viscous body crossflow. This simplified method somewhat underestimates the incremental coefficient in the higher range of angles of attack. The discrepancy indicates a differential loading between wing panels which is not taken into account. As pointed out in the previous section, a differential wing loading acts on the body when the wing is asymmetrically located (high or low) on the body. To some extent a differential wing loading can also result between sweptback wing panels because of unequal sweepback of their leading edges when in an attitude of yaw. This effect, which is not taken into account in the method, in conjunction with the approximate account which is taken of viscous crossflow suppression might explain the lack of better agreement between estimate and experiment.

Experimental and theoretical values for incremental side-force coefficients contributed by wings of various plan forms in high and low location on a body are presented in figures 16(b) through (i). Agreement between estimated and experimental values is generally good. This good correlation is somewhat surprising since the factor $k(\alpha)$ in equation (28) applies strictly to two-dimensional wings and, in particular, to wings with unswept leading edges, whereas the experimental data apply to wing-body configurations, among which the wing sweepback varies greatly. The effect of wing sweepback is twofold: (1) Sweepback reduces the effect of $k(\alpha)$ primarily by reducing the effective value of η_w in equation (27). (An approximate estimate by linearized wing theory for a sweptback sonic leading-edge case indicates a decrease in this term by about 35 percent below that of the two-dimensional value.) (2) The unequal panel loading occurring with yawed, sweptback wings generates additional differential load on the body, tending to compensate for the reduced value of the factor η_w . No attempt is made herein to estimate the magnitude of the wing sweepback effects. In view of the correlations of figure 16, it appears that in lieu of refined methods, equation (28) can be applied within ± 20 -percent accuracy to combinations having sweptback, but supersonic leading edges.

Correlation of experimental and estimated yawing moments (fig. 17) are somewhat inconclusive, since, for the conventional wing locations considered here, the center of the wing-body interference pressures is close to the moment reference point, resulting in small values for yawing moment. These small yawing moments are possibly no larger than the yawing moments of the wing alone (neglected in the method). Furthermore, as stated in the body-alone discussion, the center of pressure of the body

crossflow loading is not accurately known. Thus, exact knowledge of wing effects on the body crossflow load distribution is precluded. Estimates of the wing-body interference moments by the methods presented is warranted in cases where the mid-point of the wing root chord is substantially displaced from the moment reference point. Previously it was shown that large gains in side-force coefficients over that of the body alone occur with angle of attack if the wing is located in a high body position. This increased side force produces no significant stability increases in the cases considered since the force is confined to the vicinity of the wing root chord and near the moment center reference. Modifying a wing plan form so that the root chord is displaced rearward without changing the center-of-pressure location is a means by which wing-body interference can be exploited for increased directional stability. Such a wing compared with a conventional wing in combination with a body is shown:

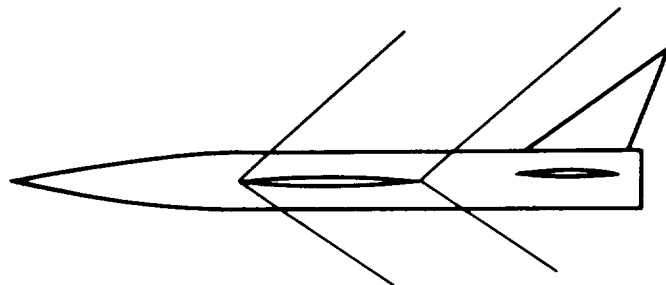


Sketch (g)

Body-Wing-Tail Combinations

Uncoupled configurations.- The previous sections considered separately body-tail configurations and body-wing configurations. For a certain class of body-wing-tail configurations, it is only necessary to add the wing-body interference terms to the body-tail coefficients to determine the coefficients of a body in combination with a tail and a wing at low angles of inclination. The class of aircraft to which this procedure

applies is termed the uncoupled wing-tail configuration. An illustration of this class is shown in sketch (h). If a body section separates the



Sketch (h)

wing from the empennage as indicated so that the Mach lines emanating from the wing (containing the wing pressure fields) do not impinge on the tail surfaces, the airplane is classed as uncoupled. Actually, an additional influence of the wing exists because of changes in sidewash caused by the wing addition. The altered sidewash persists to some extent aft of the trailing-edge Mach lines. This wing influence on the tail was not considered in the method for the sake of simplicity since the accuracy of the estimates was not seriously compromised as will be shown. The assumption of the lack of wing-tail interference applies to the condition of low angle of attack and sideslip. Potential flow uncoupling does not preclude wing-tail interference in general. When the wing is upstream of the tail, the effect of wing vortices on the tail can be significant and should be considered. To this end, wing vortex strengths and positions can be determined by an obvious extension of the procedure of reference 13. Theoretical body vortex positions, as affected by the presence of the wing, are not at present amenable to ready solution for the general case of combined sideslip and angle of attack. However, when sideslip angle is small, the approximate effect of the wing on body vortex strength and displacement can be taken into account by the methods of reference 12.

Uncoupled configurations in pure sideslip.- The incremental side-force and yawing-moment coefficients due to the addition of an upper tail to a wing-body configuration are

$$C_{Y_{BWV}} - C_{Y_{BW}} = K_V(B) C_{Y_V} \quad (30)$$

and

$$C_{n_{BWV}} - C_{n_{BW}} = \frac{\bar{l}_V - \bar{l}_M}{2s_W} K_V(B) C_{Y_V} \quad (31)$$

The incremental coefficients of body-wing-tail combinations including a ventral fin are

$$C_{Y_{BWWU}} - C_{Y_{BW}} = K_V(B)C_{Y_V} + K_{U(BV)}C_{Y_U} \quad (32)$$

and

$$C_{n_{BWWU}} - C_{n_{BW}} = \frac{\bar{l}_V - l_M}{2s_W} K_V(B)C_{Y_V} + \frac{\bar{l}_U - l_M}{2s_W} K_{U(BV)}C_{Y_U} \quad (33)$$

Uncoupled configurations in combined sideslip and angle of attack.- The effect of angle of attack on the incremental coefficient contributions of an upper tail to a wing-body combination is taken into account by additional cross-coupling and vortex terms. The side-force and yawing-moment coefficient contributions of an upper tail to a body-wing combination are

$$C_{Y_{BWW}} - C_{Y_{BW}} = \left[K_V(B) - \frac{K_{\phi\alpha}}{\tan \epsilon_V} \right] C_{Y_V} + C_{Y_V(\Gamma_B)} \quad (34)$$

and

$$C_{n_{BWW}} - C_{n_{BW}} = \frac{\bar{l}_V - l_M}{2s_W} \left[K_V(B) - \frac{K_{\phi\alpha}}{\tan \epsilon_V} \right] C_{Y_V} + C_{Y_V(\Gamma_B)} \quad (35)$$

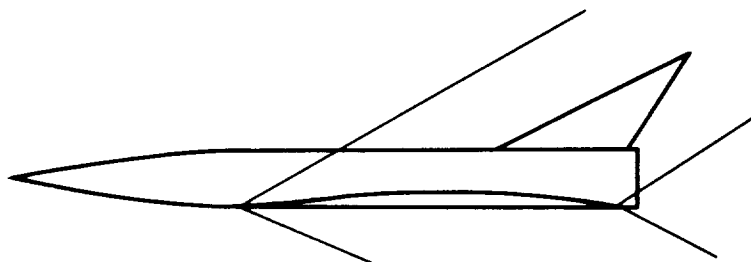
The incremental coefficients applying to body-wing-tail configurations which include a ventral fin are

$$C_{Y_{BWWU}} - C_{Y_{BW}} = \left[K_V(B) - \frac{K_{\phi\alpha}}{\tan \epsilon_V} \right] C_{Y_V} + C_{Y_V(\Gamma_B)} + \left[K_{U(BV)} + \frac{K_{\phi\alpha}}{\tan \epsilon_U} \right] C_{Y_U} + C_{Y_U(\Gamma_B)} \quad (36)$$

and

$$C_{n_{BWWU}} - C_{n_{BW}} = \frac{\bar{l}_V - l_M}{2s_W} \left[K_V(B) - \frac{K_{\phi\alpha}}{\tan \epsilon_V} \right] C_{Y_V} + C_{Y_V(\Gamma_B)} + \frac{\bar{l}_U - l_M}{2s_W} \left[K_{U(BV)} + \frac{K_{\phi\alpha}}{\tan \epsilon_U} \right] C_{Y_U} + C_{Y_U(\Gamma_B)} \quad (37)$$

Closely coupled configurations.- On many aircraft the wing is in such proximity to the empennage that the tail surfaces are totally enveloped by the wing flow field. Configurations of this type are classed as closely coupled wing-tails, as typified in the following sketch:



Sketch (i)

Closely coupled configurations in pure sideslip.- In accordance with figure 2, the side-force coefficient contribution of an upper tail to a body-wing configuration when total coupling exists, is

$$C_{Y_{BWV}} - C_{Y_{BW}} = K_V(BW) C_{Y_V} \quad (38)$$

The corresponding incremental yawing-moment coefficient is

$$C_{n_{BWV}} - C_{n_{BW}} = \frac{\bar{l}_V - l_M}{2s_W} K_V(BW) C_{Y_V} \quad (39)$$

The incremental coefficients pertaining to combinations including a ventral fin are

$$C_{Y_{BWVU}} - C_{Y_{BW}} = K_V(BW) C_{Y_V} + K_U(BWV) C_{Y_U} \quad (40)$$

and

$$C_{n_{BWVU}} - C_{n_{BW}} = \frac{\bar{l}_V - l_M}{2s_W} K_V(BW) C_{Y_V} + \frac{\bar{l}_U - l_M}{2s_W} K_U(BWV) C_{Y_U} \quad (41)$$

Values for the K factors are given in figure 18 as a function of body radius to tail semispan ratio. This figure gives the interference coefficients for mid, low, and high body locations for a wing having a ratio of semispan to body radius of 5. More extensive sets of interference coefficients are presented in reference 6, wherein the effect of wing span and body ellipticity as variables is considered.

Closely coupled configurations in combined sideslip and angle of attack.- Two distinct interference effects between wing and tail are caused by angle of attack for closely coupled configurations. One of these, the effect of the wing on body vortices, has been pointed out in connection with uncoupled wing-tail configurations. The second is the change in the side-force coefficient of the tail panel when it is in the

wing flow field. This latter effect can be approximately taken into account by effectiveness factor η_W discussed in the body-wing section. For a closely coupled wing and tail, the effects of wing vortices are precluded since the wing vortex wake is downstream of the empennage.

The side-force and yawing-moment coefficient increments due to the addition of a tail to a body-wing combination in combined angle of attack and sideslip are

$$C_{Y_{BWV}} - C_{Y_{BW}} = \left\{ \left[K_V(BW) - \frac{K_{\phi\alpha}}{\tan \epsilon_V} \right] C_{Y_V} + C_{Y_V(\Gamma_B)} \right\} \eta_W \quad (42)$$

and

$$C_{n_{BWV}} - C_{n_{BW}} = \frac{\bar{l}_V - l_M}{2s_W} \left\{ \left[K_V(BW) - \frac{K_{\phi\alpha}}{\tan \epsilon_V} \right] C_{Y_V} + C_{Y_V(\Gamma_B)} \right\} \eta_W \quad (43)$$

The increments for a body-wing-tail configuration including a ventral fin are

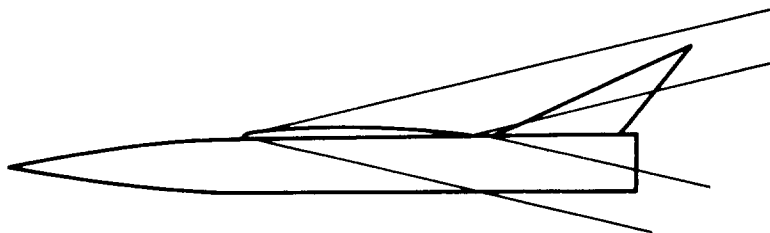
$$C_{Y_{BWWU}} - C_{Y_{BW}} = \left\{ \left[K_V(BW) - \frac{K_{\phi\alpha}}{\tan \epsilon_V} \right] C_{Y_V} + C_{Y_V(\Gamma_B)} \right\} \eta_W + \\ \left\{ \left[K_U(BWV) + \frac{K_{\phi\alpha}}{\tan \epsilon_U} \right] C_{Y_U} + C_{Y_U(\Gamma_B)} \right\} \eta_W \quad (44)$$

and

$$C_{n_{BWWU}} - C_{n_{BW}} = \frac{\bar{l}_V - l_M}{2s_W} \left\{ \left[K_V(BW) - \frac{K_{\phi\alpha}}{\tan \epsilon_V} \right] C_{Y_V} + C_{Y_V(\Gamma_B)} \right\} \eta_W + \\ \frac{\bar{l}_U - l_M}{2s_W} \left\{ \left[K_U(BWV) + \frac{K_{\phi\alpha}}{\tan \epsilon_U} \right] C_{Y_U} + C_{Y_U(\Gamma_B)} \right\} \eta_W \quad (45)$$

The effectiveness factor η_W is plotted as a function of angle of attack for various Mach numbers in figure 19. The use of this figure is made clear by the example on figure 19(a). A suitably scaled outline of an airplane with its root chord length coinciding with length c_r on the chart locates the tail in the proper influence zones. For the example shown values of $\eta_W = 0.96$ for the upper tail and $\eta_W = 1.04$ for the ventral fin are determined by integration of η_W with tail area in each influence zone.

Partially coupled configurations.- Frequently, body-wing-tail configurations have partial coupling between wing and tail. In fact, a configuration uncoupled at low Mach numbers may become partially coupled at high Mach numbers. Sketch (j) illustrates an example of partial



Sketch (j)

coupling. In this class of configurations, the extent of tail area affected by the wing depends not only on wing location but on angle of attack as well. The method of calculating interference coefficients due to the addition of the tail requires only a simple modification to the interference coefficient used in the equation which applies to closely coupled configurations. The interference coefficient $K_V(BW)$ is modified as in the method of reference 6. An effective K' is determined by the tail area, $S_V(BW)$, lying in the wing expansion (or compression) field subject to influence $K_V(BW)$ and that of the tail area, $S_V(B)$, lying out of this field and subject to influence $K_V(B)$

$$K' = \frac{K_V(BW)S_V(BW) + K_V(B)S_V(B)}{S_V} \quad (46)$$

Wing vortex effects are generally negligible for partially coupled wing-tail configurations.

Comparison of estimate and experiment.- Estimated and experimental side-force and yawing-moment coefficients of body-wing-tail configurations are compared on the basis of the difference between the coefficient value for the body-wing-tail combination and that of the body-wing combination. This difference is the measure of the tail effectiveness in the presence of a winged body. Discussion of the comparison of experiment and estimate is confined to side-force coefficient correlation since the degree of corresponding yawing-moment correlation follows in close parallel. Estimated and experimental values are presented in figures 20, 21, and 22.

Except in one case (fig. 20(d)) the configurations all have a forebody extending forward of the wing. Body vorticity therefore affects the tail effectiveness and is taken into account in the theory. The

effect of the wing on body vortices is taken into account by an approximation to the method of reference 1. It is assumed here that both vortex strengths and positions are those about a body foreshortened by the length of the wing root chord. This approximation then neglects the effects of the wing flow field on vortex position; however, the error introduced at small sideslip angles is small. Confirmation in this regard is indicated in that the correlation of experiment and estimate (figs. 20(a) through (c)) is generally good at $\beta = 5.1^\circ$ and poor at $\beta = 10^\circ$. Poor correlation at the larger sideslip angles can be expected since 10° of sideslip is well into the angle range where viscous lateral crossflow effects become important. The wing does not suppress and may even augment body vortices generated by "strong" sidewash. For instance, data for the low wing configurations at $\beta = 10^\circ$ indicate a large difference between experiment and estimate. Experimental data for the high wing configuration at $\beta = 10^\circ$ is, however, in better accord with estimate. The strongest influence of the wing on body vortices at large angles of sideslip is thus associated with low wing position.

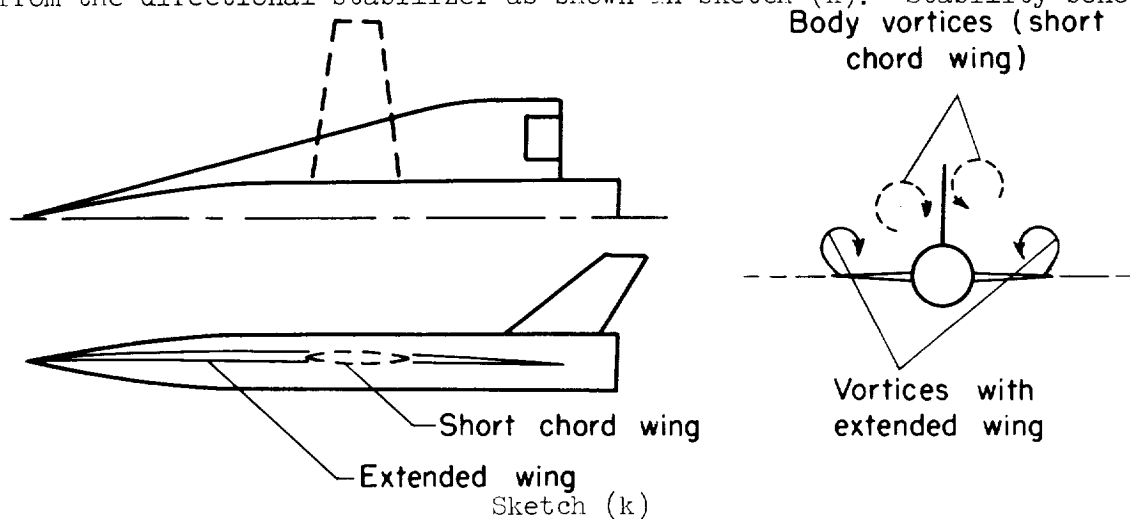
The wing wake function η_W , based on two-dimensional shock-expansion theory, cannot be expected to apply to wing plan forms of low aspect ratio. This consideration was discussed briefly in the section on body-wing interference in connection with highly swept wings. A case in point is involved in the correlation of experiment and estimate in figure 20(d). It is to be noted that the wing plan form is of low aspect ratio and has subsonic leading edges at the test Mach number. Application of the charts of figure 15, which apply strictly to two-dimensional wings, or approximately to wings with supersonic edges, is not valid for this case. A rough correction for the effect of plan form was made as follows: The ratio of the pressure coefficient along the wing center line (ignoring the presence of the body) to that of a two-dimensional wing at the same angle of attack and Mach number was determined by linear theory. The term $(1-\eta_W)$ is assumed proportional to the wing pressure coefficient. The magnitude of this term is then reduced by the ratio of finite to two-dimensional wing center-line pressures yielding an effective value for $(1-\eta_W)$ from which the wing wake function η_W is extracted. This correction applies only to the wing surface center line since flow about the finite wing is conical. It is therefore of significance that the corrected estimate gives the best correlation for the short span tail whose area is in closer "average" proximity to the wing surface than that of the long span tail. Another effect of wing plan form is indicated in the correlation presented in figure 20(e) indicating the tail contribution variation with angle of attack. The wing plan form in this case was swept forward. Because of the resulting large forward displacement of the wing tips with respect to the tail location, tip effects communicate downstream to the tail plane and relieve the "two-dimensional" nature of the wing wake field. The full compressive wing wake pressures are not then sensed by the (ventral) tail.

In the usual case of complete or partial wing-tail coupling, there are two effects of wing location on tail side-force contribution: (1) At pure sideslip, a wing mounted low on a body diverts crossflow over the top of the body which augments the sidewash at the upper tail location. This interference effect, taken into account by the interference coefficient $K_V(BW)$, results in greater incremental tail side force in the presence of low wing as compared with high wing cases. This effect of wing location is particularly evident in the correlation of estimate and experiment presented in figures 21(a) and (b). In all cases, at low angles of attack, the tail contributions are substantially greater for the low-wing configuration. (2) For a given longitudinal wing location, the wing expansion field envelopes a greater portion of the upper tail surface when the wing is mounted low on the body. As a consequence, the effectiveness of the tail then decreases more rapidly with angle of attack than if it were mounted on a high wing-body combination. Thus, at high angles, the tail contribution in the presence of a low wing may be no larger than in the presence of a high wing-body. This is particularly true at high Mach numbers ($M_\infty > 2$) as can be verified from figures 21(a) and (b). Correlation of estimates with experimental tail contributions at lower Mach numbers are presented in figures 22(a) through (d). At $M_\infty = 1.41$ the configuration of figures 22(c) and (d) falls marginally in the "uncoupled" case by the criteria of the method; thus, little effect of wing location at $\alpha = 0^\circ$ is predicted. However, experimentally a favorable effect of low wing location is clearly evident. This discrepancy between estimate and experiment indicates that wing-body effects on sidewash persist to some extent downstream of the wing trailing-edge Mach line for marginally uncoupled cases. This effect is assumed to wash out downstream of the wing trailing edge in the simplified concept presented. However, in view of the generally fair correlation between estimate and experiment, the simple criterion of coupling and the application of available K factors as presented herein and in reference 6 are justified.

The effects of wing location, of course, apply in the opposite sense in regard to ventral tails. The effect of high wing location coupled with "minimum" body vortex effects is particularly conducive to increasing ventral tail coefficients with angle of attack as shown in figures 20(e) and (f).

It may be concluded from a consideration of the combined effects of wing flow fields and body vortices that no optimum tail plan form can be specified for maximum directional stability. A short span tail is strongly affected by destabilizing body vortices but is adaptable to locations least affected by the unfavorable effects of the wing expansion field. A large span tail, conversely, is less sensitive to body vorticity but usually projects into the unfavorable region of the wing expansion field. A compromise must be made on the basis of minimizing the combined effect of both destabilizing phenomena at design Mach number.

Increased directional stability, provided sideslip angle is not large, can be gained with low-aspect-ratio wings whose root chord extends to the body nose. Such a body-wing combination generates a wake in which the vorticity is concentrated at the wing tips and is therefore "diverted" from the directional stabilizer as shown in sketch (k). Stability benefits



result even in cases of vanishingly small aspect ratio wings (strakes) as noted in references 5 and 16 because of control of body vorticity and favorable pressure changes on the forebody.

Horizontal Stabilizers

Aft located pitch stabilizers. - A detailed consideration of the effects of horizontal stabilizers on directional stability of an airplane was omitted in the present report. A systematic experimental study of horizontal stabilizer effects was not undertaken. A small aft stabilizer, simulating an all-movable pitch control, was used on two of the models and contributed no important increments in directional stability. Generally, this is not the case. Interference effects of a horizontal stabilizer incorporated in the tail on the directional coefficients of an airplane at low angles of inclination can be estimated by the methods of reference 6. The interference effects at large angles of inclination then can be accounted for by the methods discussed herein in connection with closely coupled wing-tail configurations. In application of the method for determining horizontal stabilizer interference effects, certain additional considerations must be borne in mind. These considerations may require special computations. For instance, the pitch control might be operating in the wing flow field and the superposed effects of wing and control expansion fields on the vertical tail will be involved. In this case the effective control angle can be modified by the wing flow field and should be taken into account.

The vertical location of an aft mounted pitch stabilizer is affected by optimum longitudinal stability considerations which might not be consistent with optimum directional stability gains. These two factors must be compromised, and specific recommendations in regard to maximizing directional stability contributions of an aft located horizontal stabilizer are not justified.

Canard pitch controls.- The interference effects of canard controls on the body are identical to those of a wing on the body. The stabilizing moment arm for a canard extends forward of the airplane center of gravity and thus a negative interference force, as can be attained with a mid-wing mounted surface at high angles of attack, contributes positive directional stability. Canard locations other than mid-wing contribute positive interference forces to the body which cause negative directional stability increments.

The addition of a canard to an airplane modifies the body wake affecting the vertical stabilizer. This modified wake can improve the stability contribution of twin stabilizers (ref. 17) but generally decreases the effectiveness of a single stabilizer.

CONCLUSIONS

Correlation between estimated and experimental values for side-force and yawing-moment coefficients of supersonic aircraft configurations presented herein support the following conclusions:

1. The estimation procedure is sufficiently reliable and consistent to enable reasonably accurate prediction to be made of the static stability of proposed aircraft configurations.
2. Lack of good correlation between the present method and experiment in certain instances at large sideslip angle is traceable to the effects of the wing on body vortices. Further experimental and theoretical investigation on body-wing vortices at large sideslip angles is needed for a more complete estimation procedure.
3. The study indicates that significant reduction in the decay of directional stability coefficients of supersonic airplanes, generally associated with increasing Mach number and angle of attack, can be achieved through the use of wings and stabilizers of suitable plan form and body location.

Ames Research Center
National Aeronautics and Space Administration
Moffett Field, Calif., Sept. 16, 1958

APPENDIX

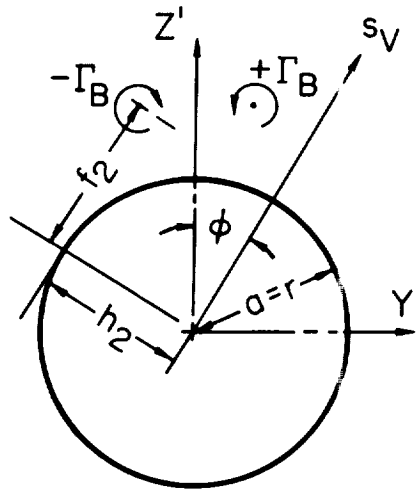
EXAMPLE CALCULATION OF BODY VORTEX EFFECT ON TAIL

Body vortex effect on the tail will be calculated for the condition $\beta = 5^\circ$, $\alpha = 12^\circ$. The center-of-pressure position of the tail at which point vortex influence is to be determined is at a distance $(x-x_S)/a = 17.6$ from the point of vortex separation. The body radius to tail semispan ratio is a/s_V or $r/s_V = 0.2$.

The effective angle of attack of the body is $\alpha' = \sqrt{\alpha^2 + \beta^2} = 13^\circ$. At $(x-x_S)/a = 17.6$ and $\alpha' = 13^\circ$, the correlation presented in reference 11 gives the approximate strengths and positions for the body vortices in the coordinate system Y', Z' where Z' is in the direction of resultant crossflow velocity, $\sqrt{v^2+w^2}$,

$$\frac{\Gamma_B}{2\pi a \sqrt{v^2+w^2}} = 1.2, \quad \frac{Z'}{a} = 1.90, \quad \frac{Y'}{a} = 0.75$$

The coordinate positions are then resolved into vertical tail reference coordinates with $\phi = \tan^{-1}(Y'/Z')$ by the following transformations as indicated in sketch (1).



Sketch (1)

$$\frac{h_1}{s_V} = \frac{a}{s_V} \left(\frac{Z'}{a} \sin \varphi - \frac{Y'}{a} \cos \varphi \right)$$

$$\frac{f_1}{s_V} = \frac{a}{s_V} \left(\frac{Z'}{a} \cos \varphi + \frac{Y'}{a} \sin \varphi \right)$$

$$\frac{h_2}{s_V} = \frac{a}{s_V} \left(\frac{Z'}{a} \sin \varphi + \frac{Y'}{a} \cos \varphi \right)$$

$$\frac{f_2}{s_V} = \frac{a}{s_V} \left(\frac{Z'}{a} \cos \varphi - \frac{Y'}{a} \sin \varphi \right)$$

The above expressions give for the positions of Γ_B , $h_1/s_V = 0.007$ and $f_1/s_V = 0.413$, and $h_2/s_V = 0.285$ and $f_2/s_V = 0.294$. Corresponding values for i_V are, respectively, -1.9 and -1.2 as determined from figure 8. Therefore $\Delta i_t = -1.9 - (-1.2) = -0.7$. The necessary values are then in hand to determine the destabilizing side-force coefficient on the tail $C_{Y_V(\Gamma_B)}$ in terms of the side-force coefficient of the isolated tail if at an inclination of $\beta = \alpha' = 13^\circ$ as given by equation (9).

REFERENCES

1. Nielsen, Jack N., and Kaattari, George E.: The Effects of Vortex and Shock-Expansion Fields on Pitch and Yaw Instabilities of Supersonic Airplanes. IAS Preprint No. 743, 1957.
2. Jorgensen, Leland H.: Elliptic Cones Alone and With Wings at Supersonic Speeds. NACA TN 4045, 1957.
3. Spearman, M. Leroy, and Robinson, Ross B.: Investigation of the Aerodynamic Characteristics in Pitch and Sideslip of a 45° Swept-Wing Airplane Configuration With Various Vertical Locations of the Wing and Horizontal Tail. Static Lateral and Directional Stability; Mach Numbers of 1.41 and 2.01. NACA RM L57J25a, 1957.
4. Spearman, M. Leroy, Driver, Cornelius, and Hughes, William C.: Investigation of Aerodynamic Characteristics in Pitch and Sideslip of a 45° Sweptback-Wing Airplane Model With Various Vertical Locations of Wing and Horizontal Tail - Basic-Data Presentation, $M = 2.01$. NACA RM L54L06, 1955.
5. Spearman, M. Leroy: Some Factors Affecting the Static Longitudinal and Directional Stability Characteristics of Supersonic Aircraft Configurations. NACA RM L57E24a, 1957.
6. Goodwin, Frederick K., and Kaattari, George E.: Estimation of Directional Stability Derivatives at Small Angles at Subsonic and Supersonic Speeds. NASA MEMO 12-2-58A, 1958.
7. Allen, H. Julian, and Perkins, Edward W.: Characteristics of Flow Over Inclined Bodies of Revolution. NACA RM A50L07, 1951.
8. Jorgensen, Leland H.: Inclined Bodies of Various Cross Sections at Supersonic Speeds. NASA MEMO 10-3-58A, 1958.
9. Polhamus, Edward C.: Effect of Flow Incidence and Reynolds Number on Low-Speed Aerodynamic Characteristics of Several Noncircular Cylinders With Applications to Directional Stability and Spinning. NACA TN 4176, 1957.
10. Gowen, Forrest E., and Perkins, Edward W.: Drag of Circular Cylinders for a Wide Range of Reynolds Numbers and Mach Numbers. NACA TN 2960, 1953.
11. Spahr, J. Richard: Contribution of the Wing Panels to the Forces and Moments of Supersonic Wing-Body Combinations at Combined Angles. NACA TN 4146, 1957.

12. Nielsen, Jack N.: The Effects of Body Vortices and the Wing Shock-Expansion Field on the Pitch-Up Characteristics of Supersonic Airplanes. NACA RM A57L23, 1958.
13. Pitts, William C., Nielsen, Jack N., and Kaattari, George E.: Lift and Center of Pressure of Wing-Body-Tail Combinations at Subsonic, Transonic, and Supersonic Speeds. NACA Rep. 1307, 1957.
14. Kaattari, George E.: Pressure Distributions on Triangular and Rectangular Wings to High Angles of Attack - Mach Numbers 2.46 and 3.36. NACA RM A54J12, 1955.
15. Ames Research Staff: Equations, Tables, and Charts for Compressible Flow. NACA Rep. 1135, 1953.
16. Driver, Cornelius: Wind-Tunnel Investigation at a Mach Number of 2.01 of Forebody Strakes for Improving Directional Stability of Supersonic Aircraft. NACA RM L58C11, 1958.
17. Spearman, M. Leroy, and Driver, Cornelius: Longitudinal and Lateral Stability and Control Characteristics at Mach Number 2.01 of a 60° Delta-Wing Airplane Configuration Equipped With a Canard Control and With Wing Trailing-Edge Flap Controls. NACA RM L58A20, 1958.

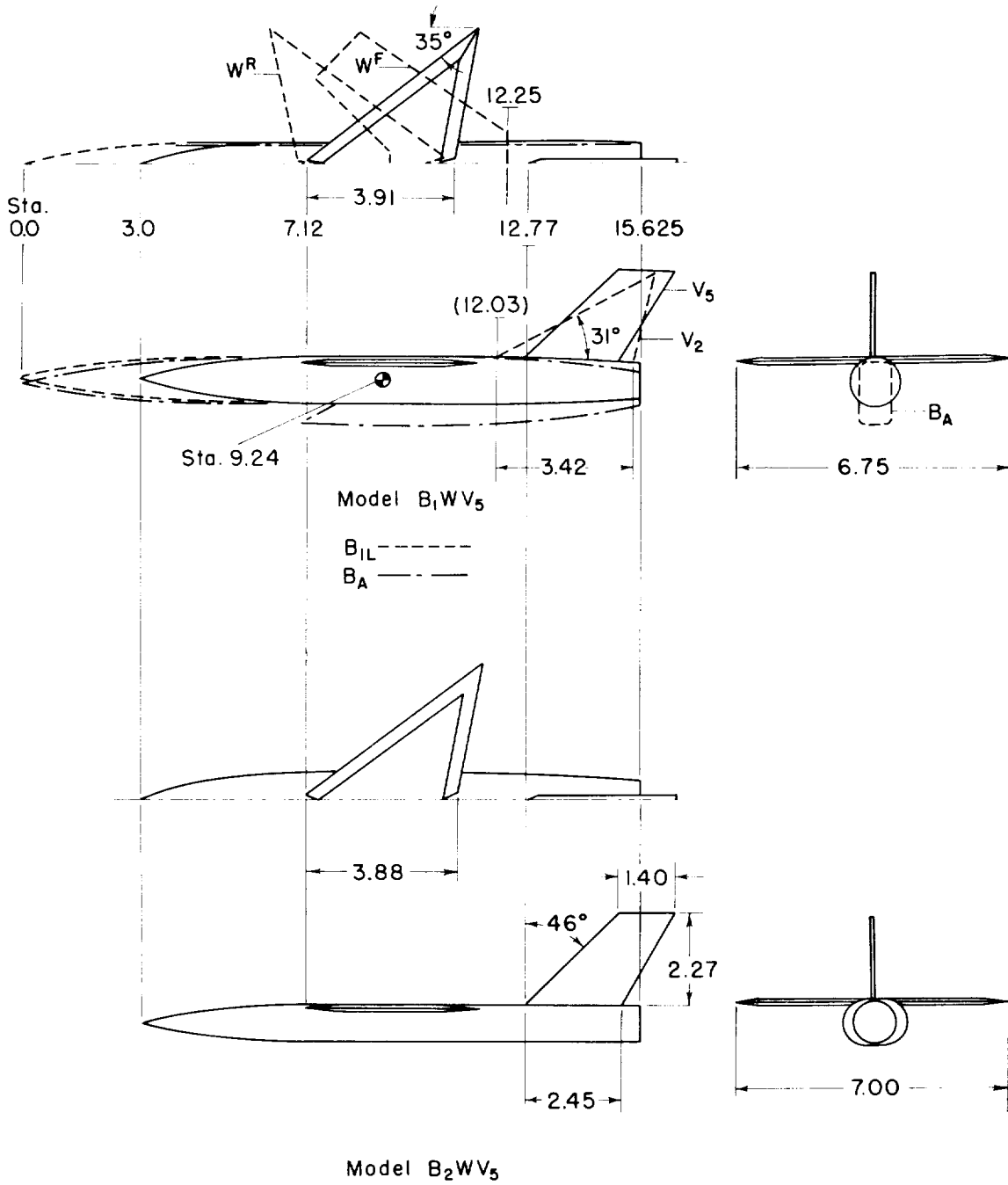


Figure 1.- Model dimensions. (All dimensions in inches. Body coordinates given in table I.)

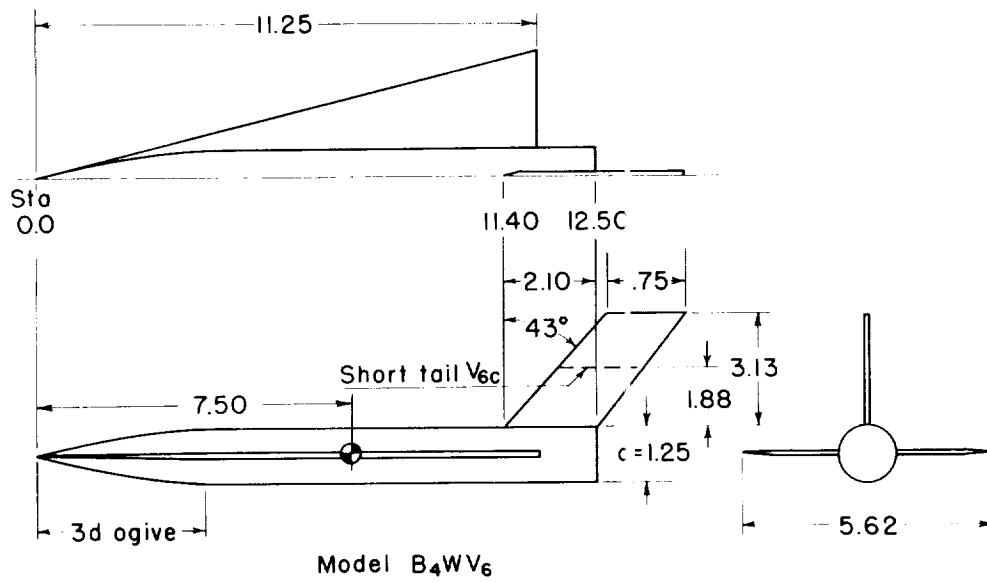
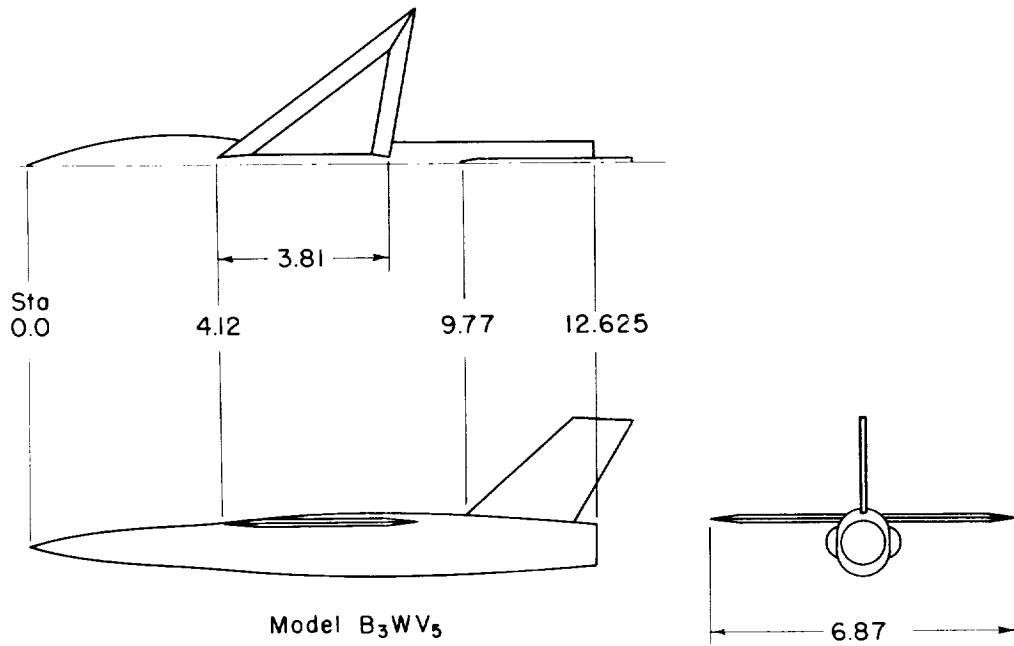
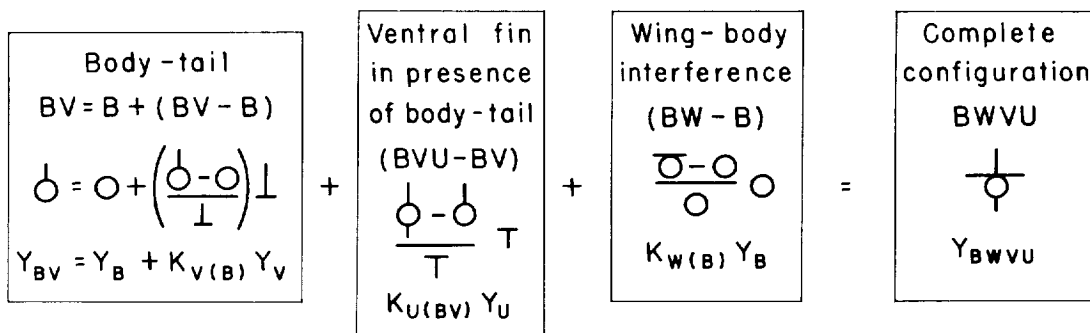
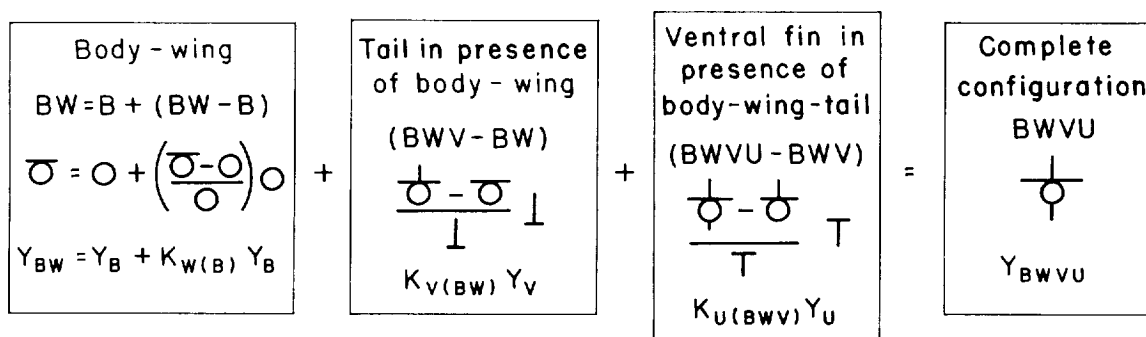


Figure 1.- Concluded.



(a) Uncoupled wing-tail configurations.



(b) Closely coupled wing-tail configurations.

Figure 2.- Symbolic definition and order of application of interference coefficients K used in determining side force.

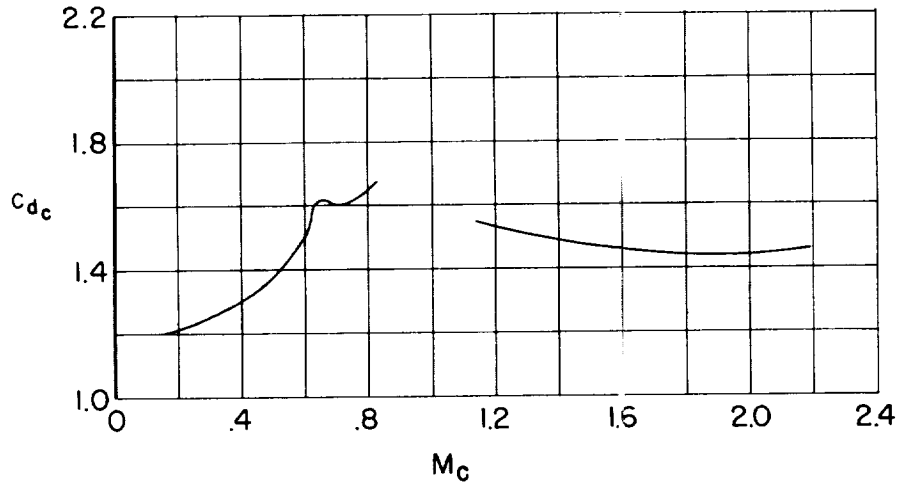


Figure 3.- Measured crossflow drag coefficient c_{dc} as a function of crossflow Mach number M_c .

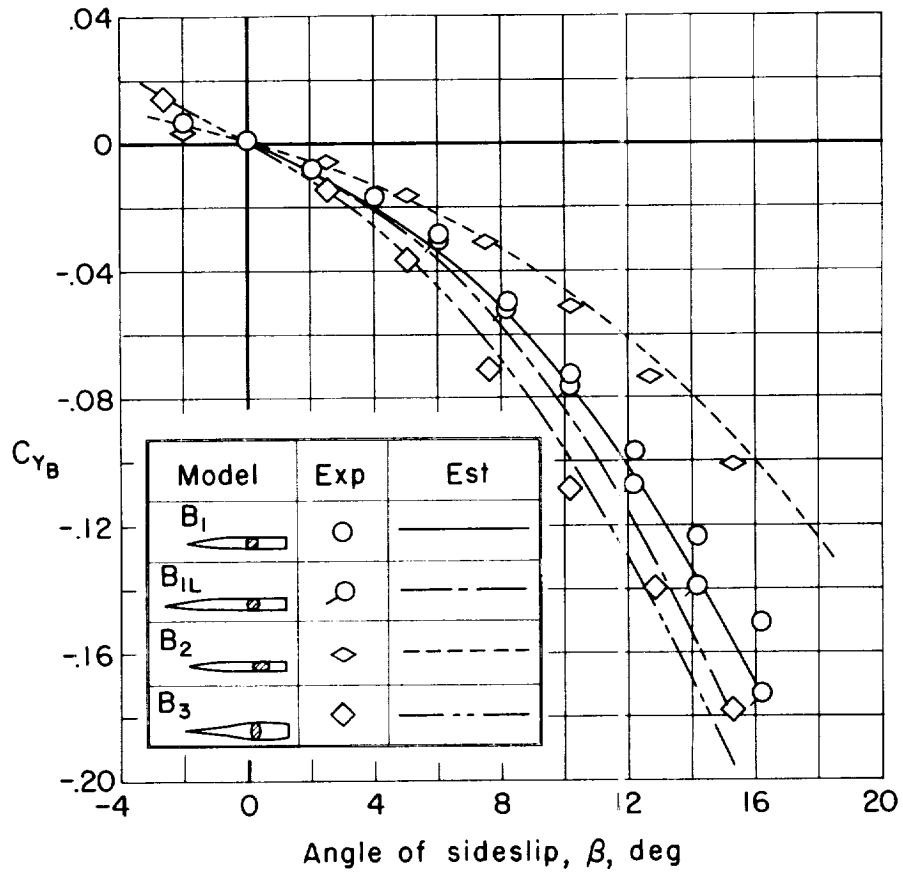


Figure 4.- Variation of side-force coefficient C_y of bodies with angle of sideslip; $M_\infty = 2.94$.

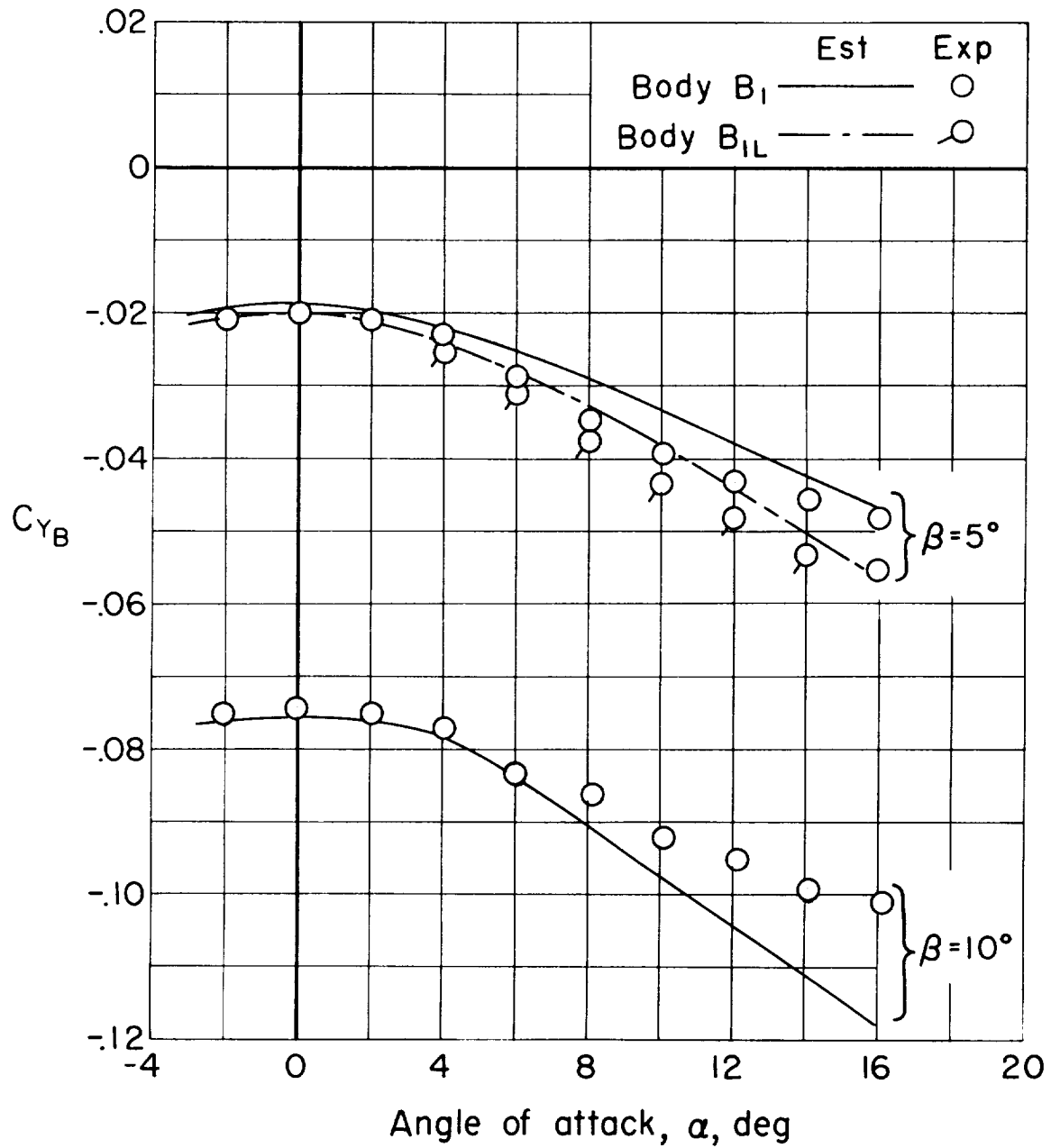


Figure 5.- Variation of side-force coefficient C_{YB} of circular bodies with angle of attack.

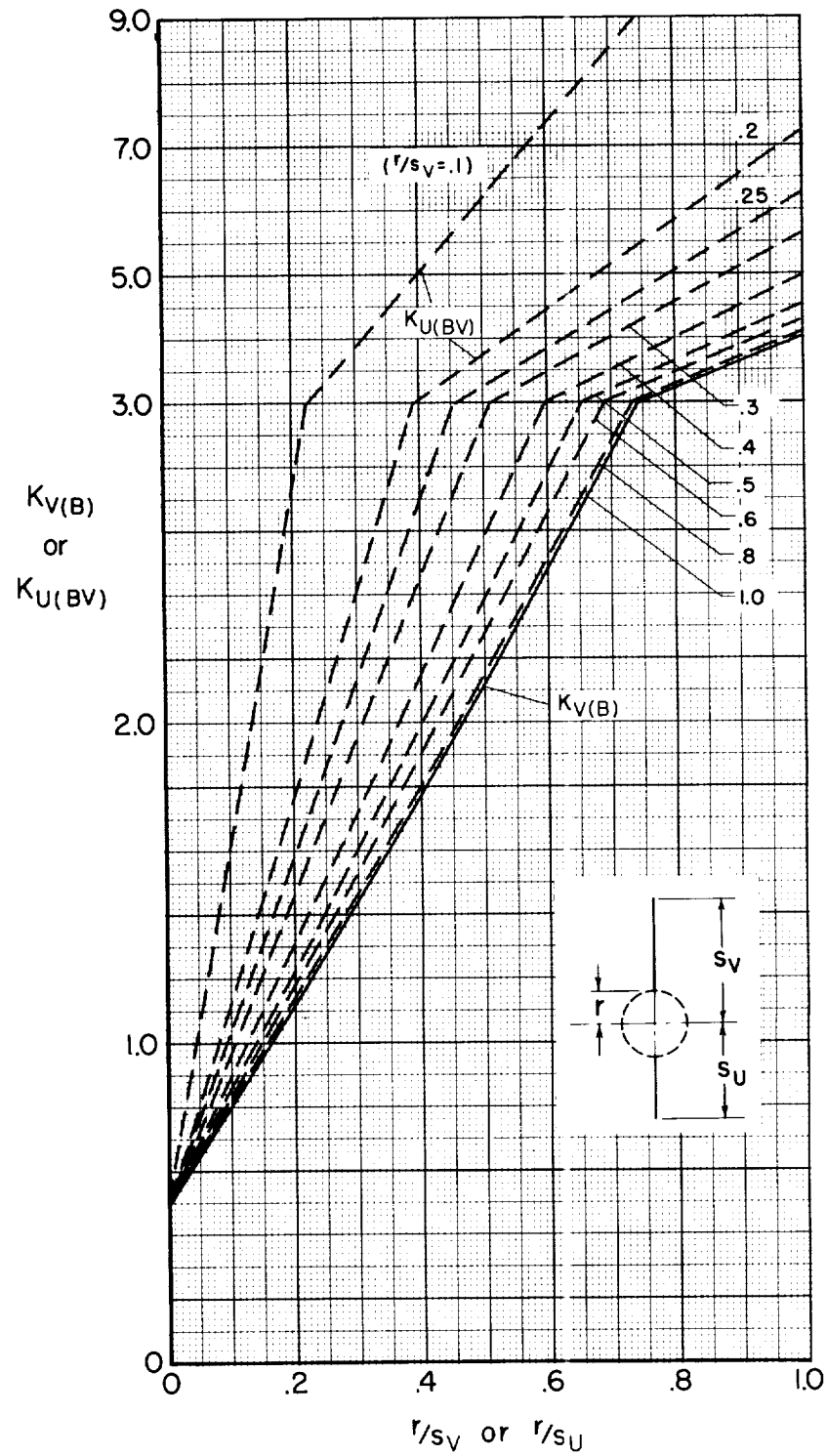


Figure 6.- Interference coefficient K chart for vertical tails and ventral fins.

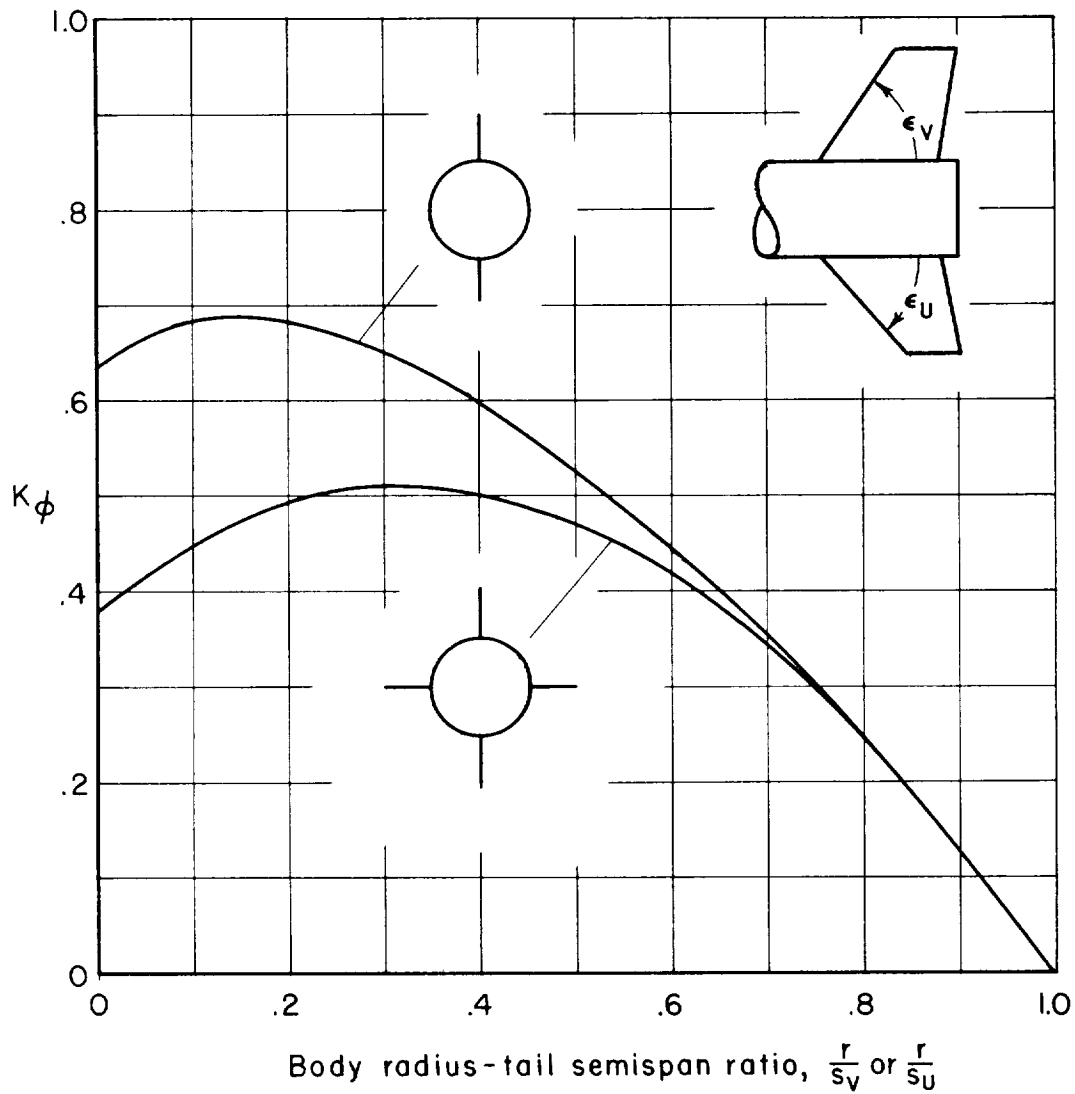


Figure 7.- Cross-coupling factor K_ϕ as a function of ratio of body radius to tail semispan, r/s_v or r/s_u .

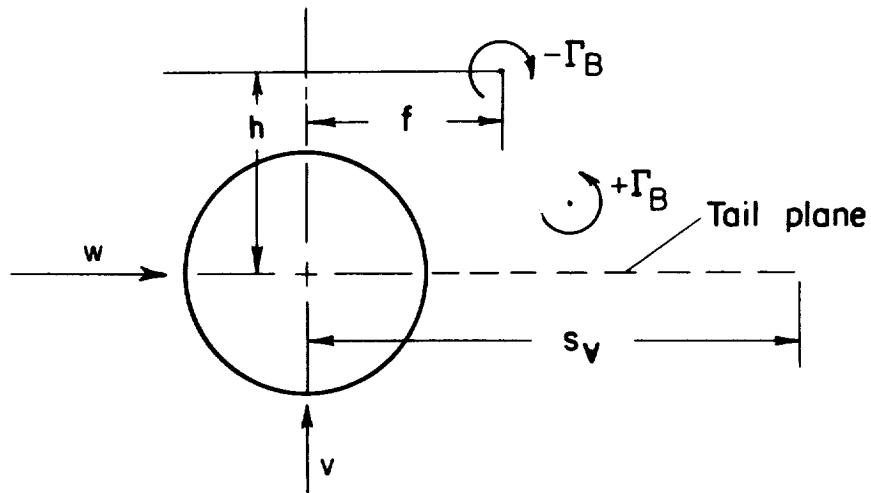
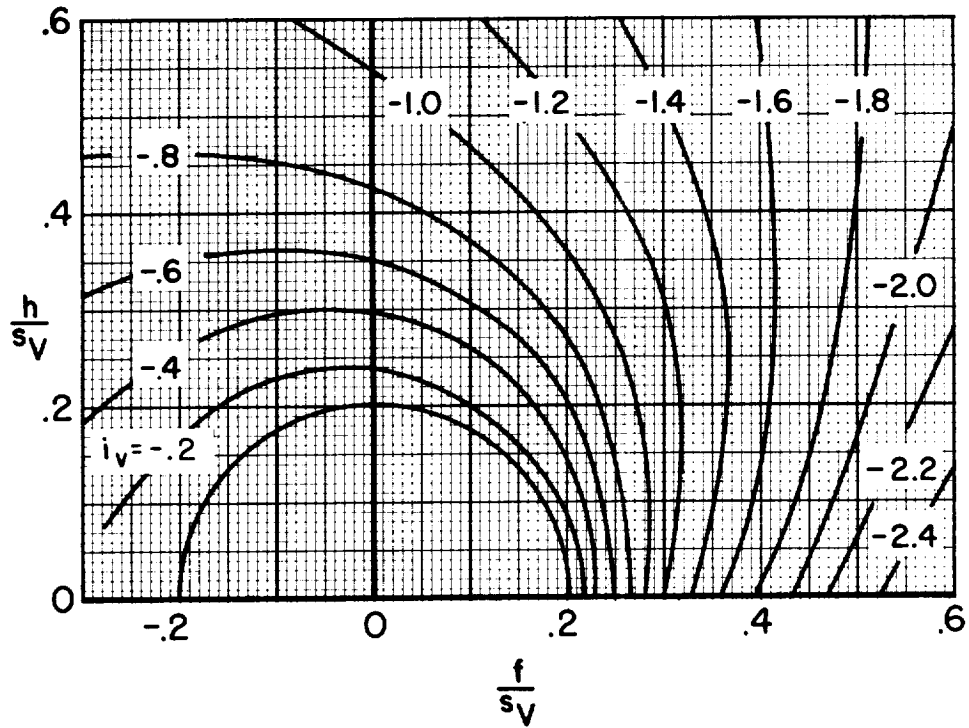


Figure 8.- Vortex interference chart and typical orientation of body vortices with respect to tail plane.

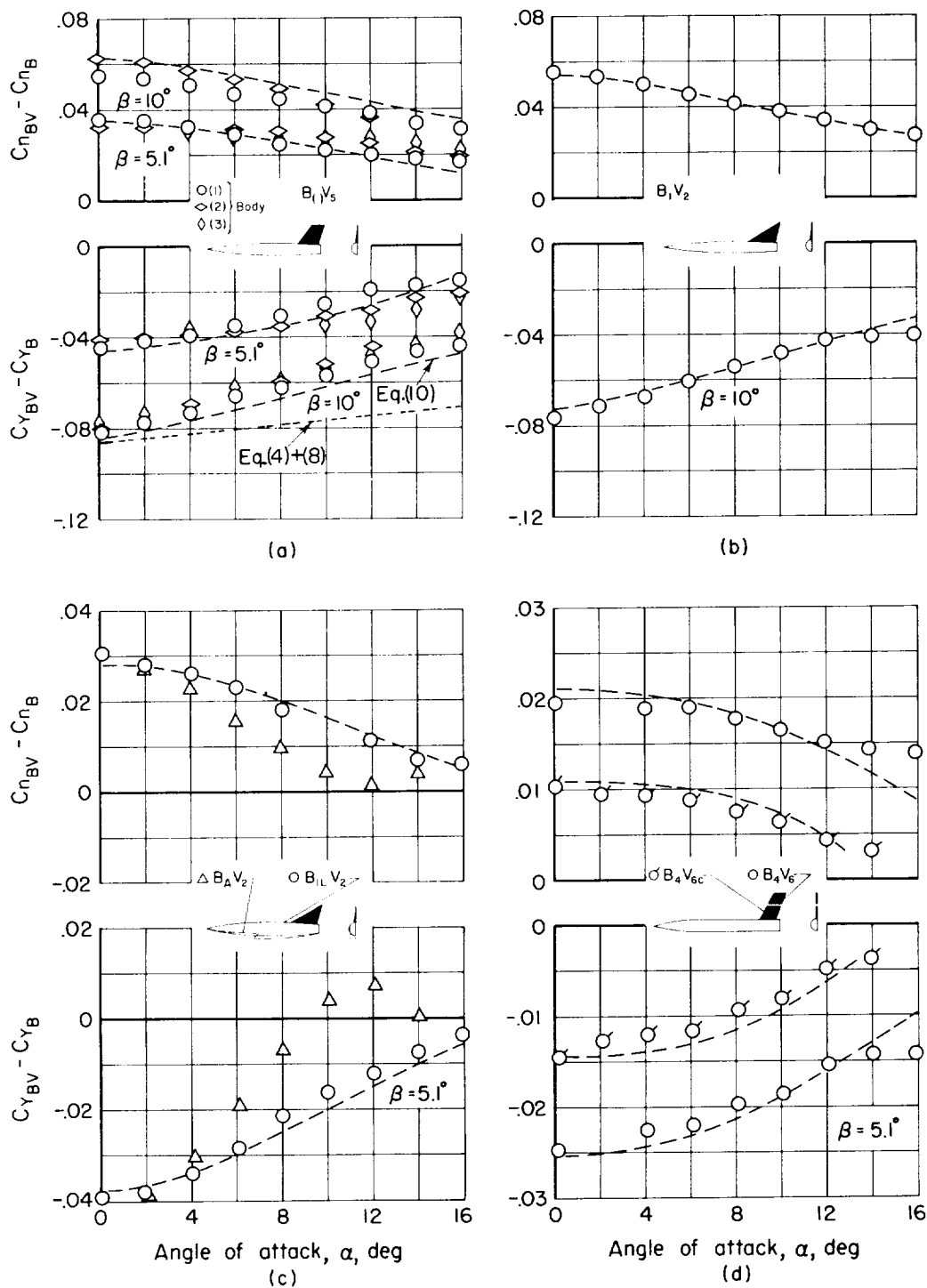


Figure 9.- Comparison of experimental and estimated directional coefficient increases due to addition of vertical tail to body $M_\infty = 2.94$.

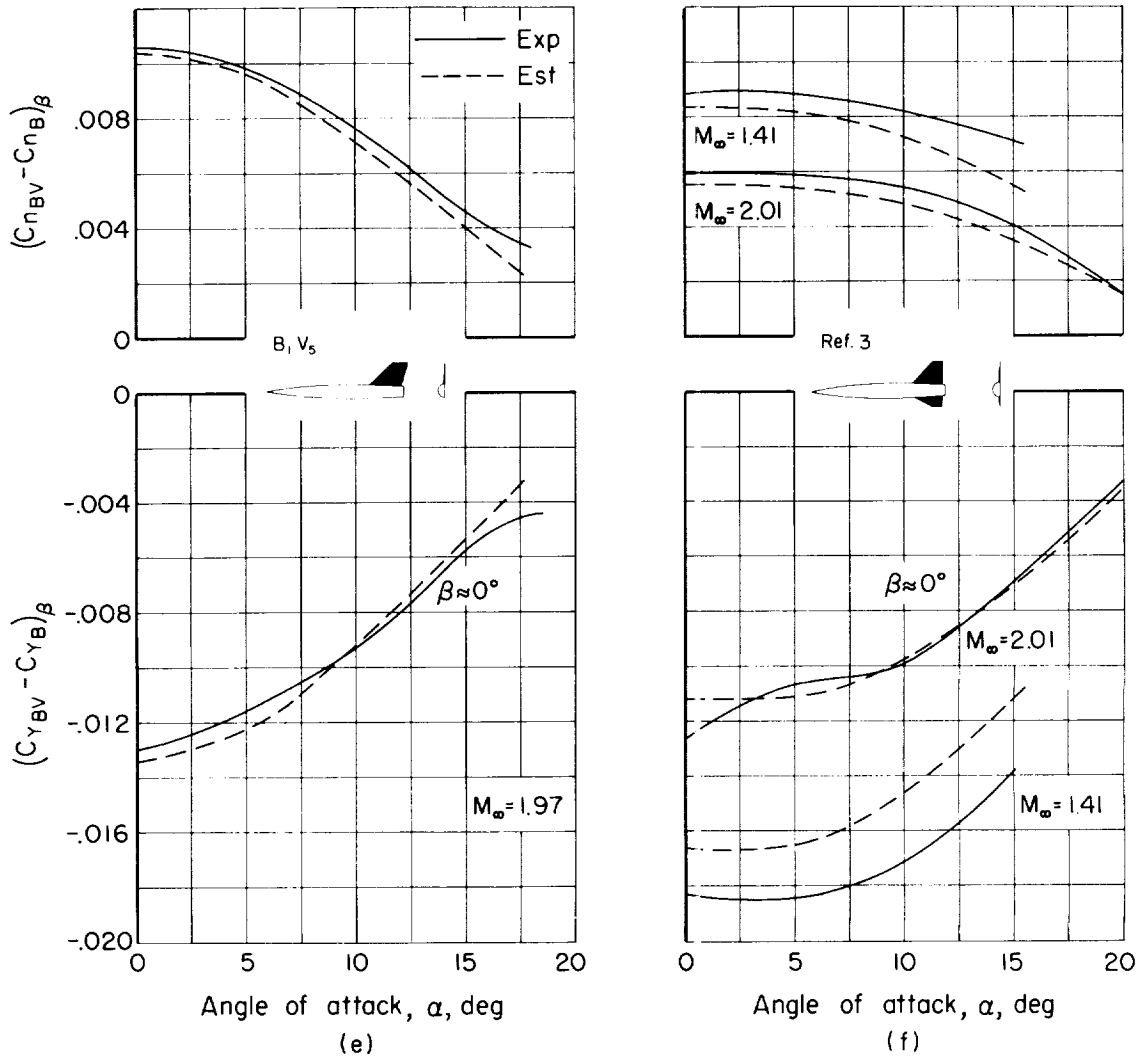


Figure 9.- Concluded.

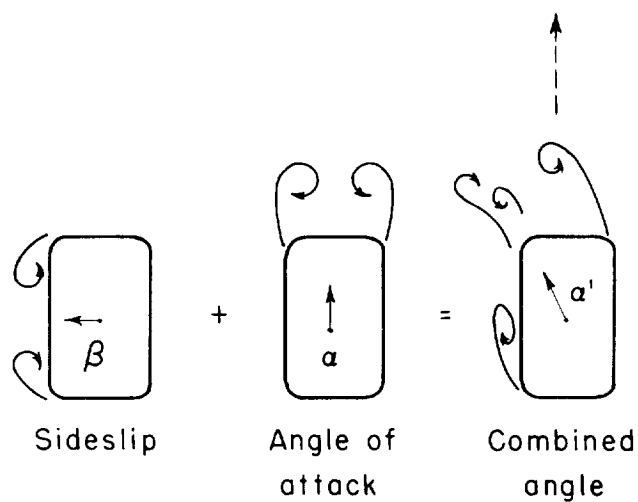
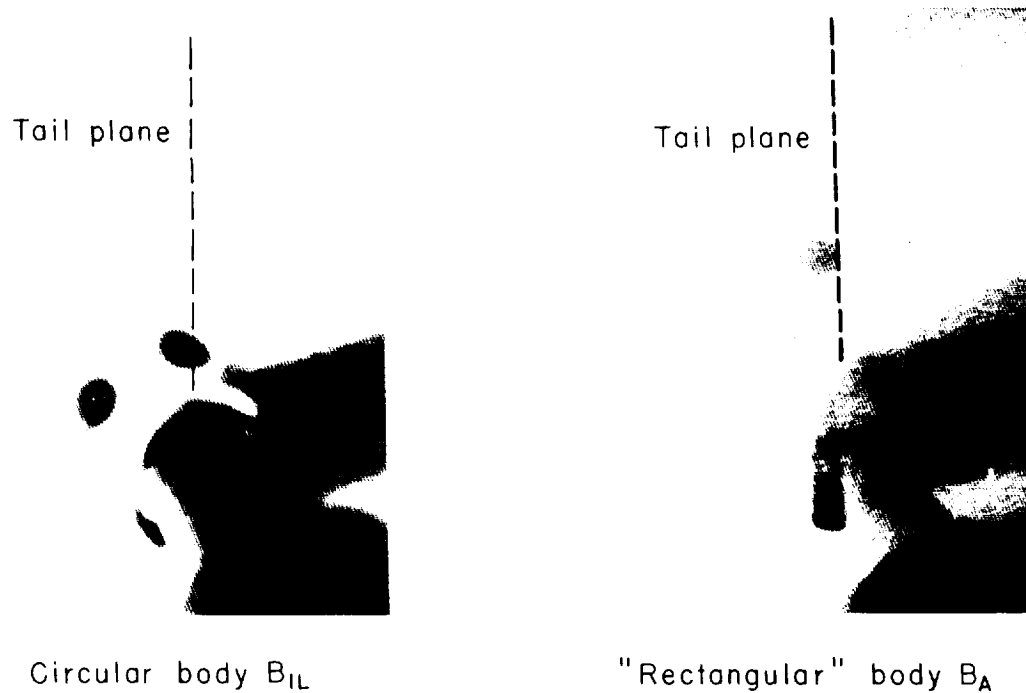


Figure 10.- Vortex formation about a circular and a rectangular body at combined angles of attack and sideslip ($\alpha = 8^\circ$, $\beta = 5^\circ$).

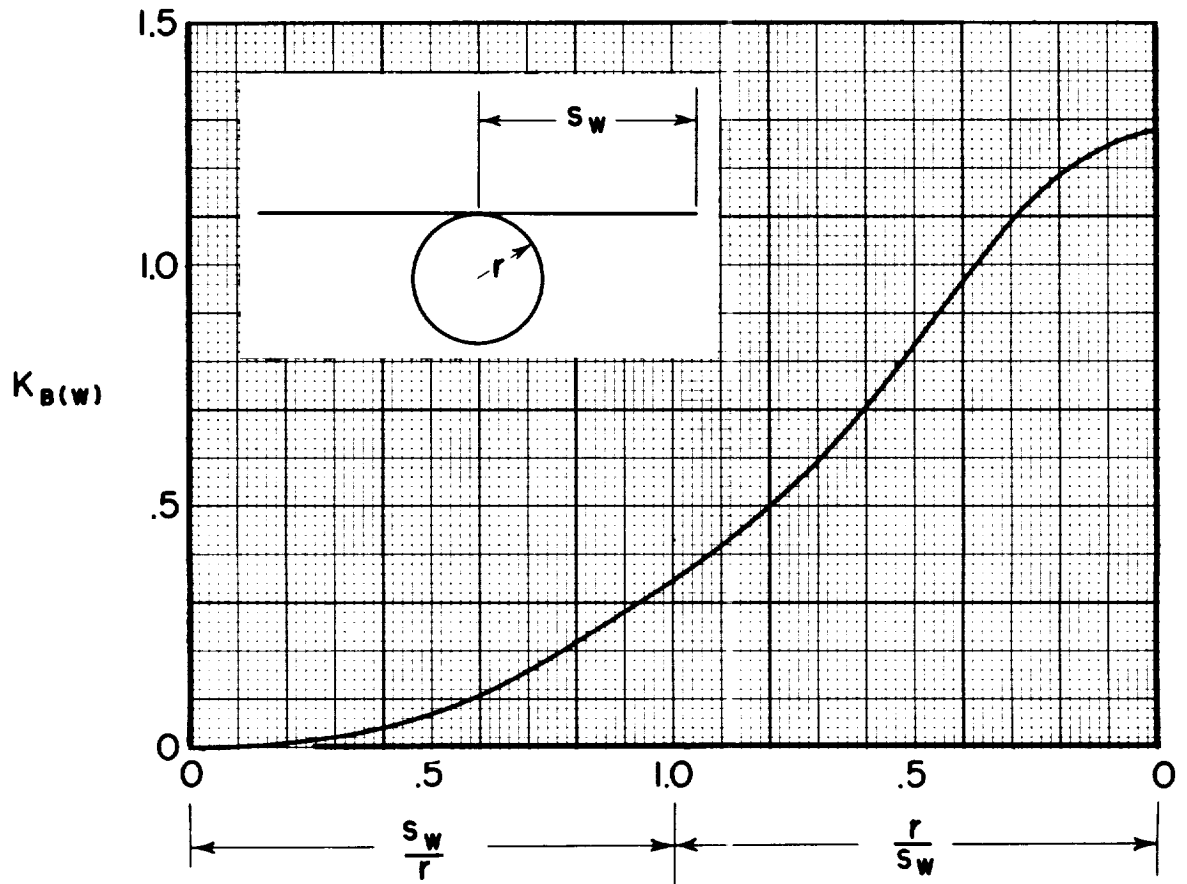


Figure 11.- Interference coefficient $K_B(w)$ for wings in a high (or low) tangent location on a body.

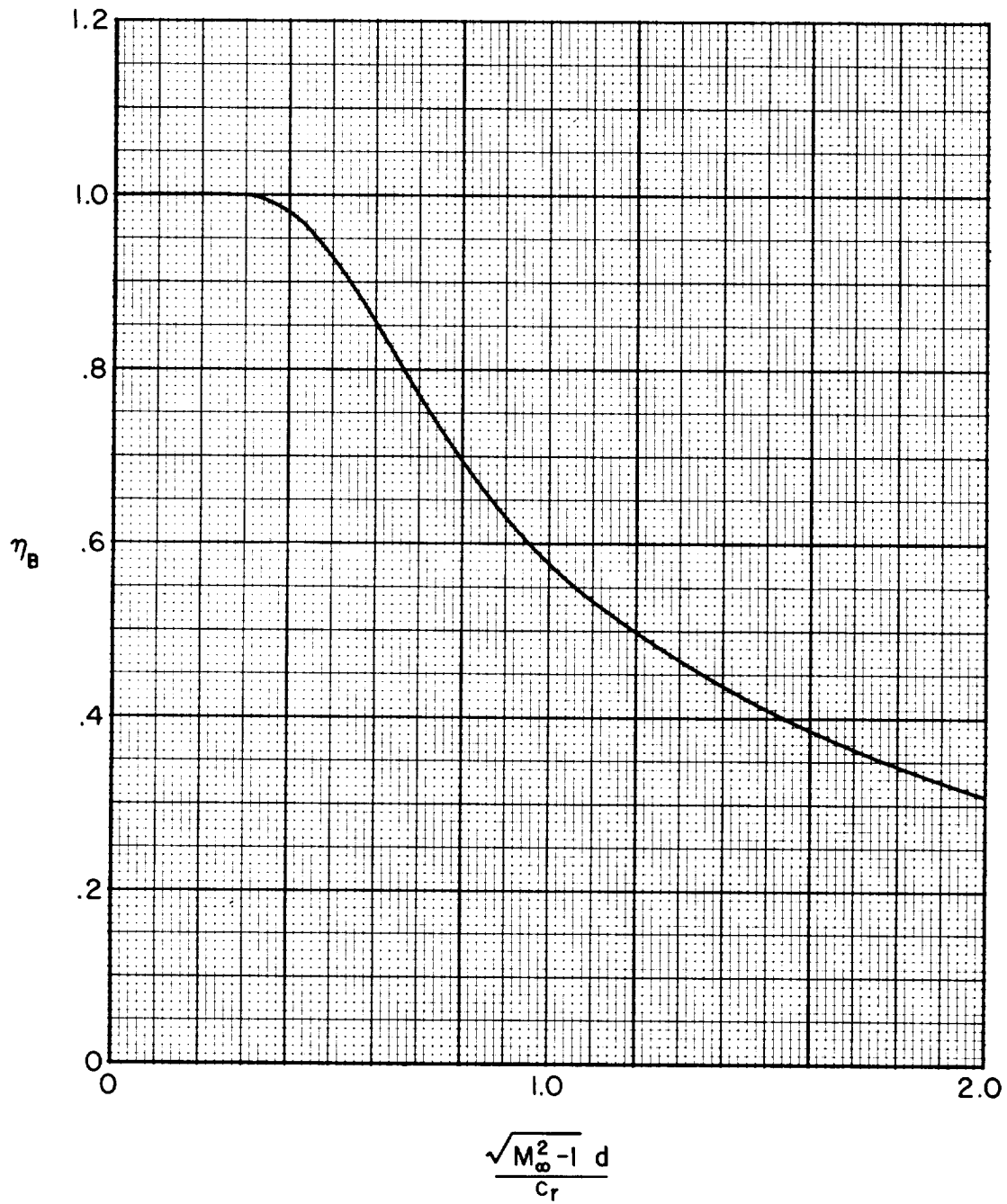


Figure 12.- Correction coefficient, η_B , to wing-body interference coefficient $K_B(W)$.

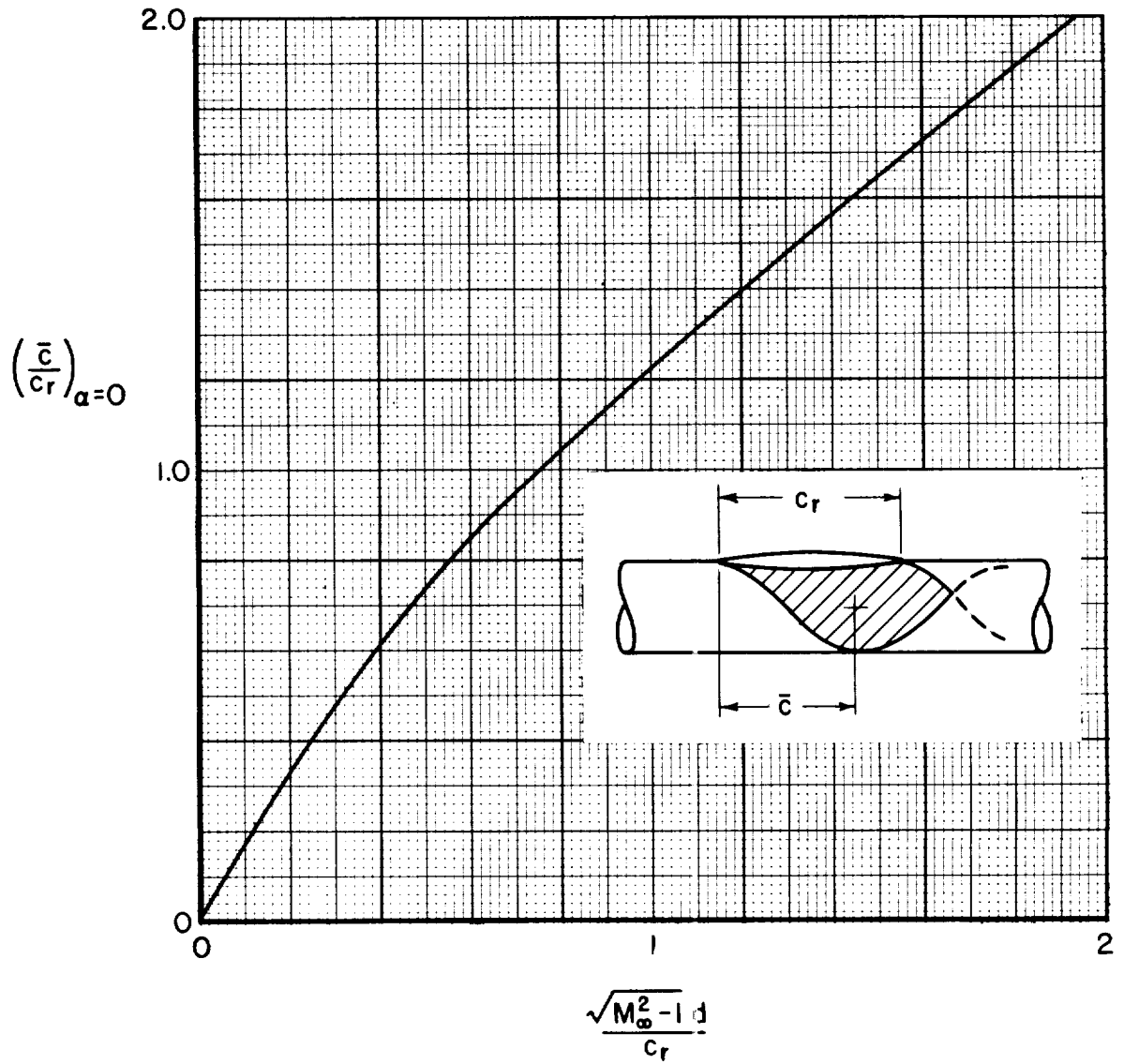
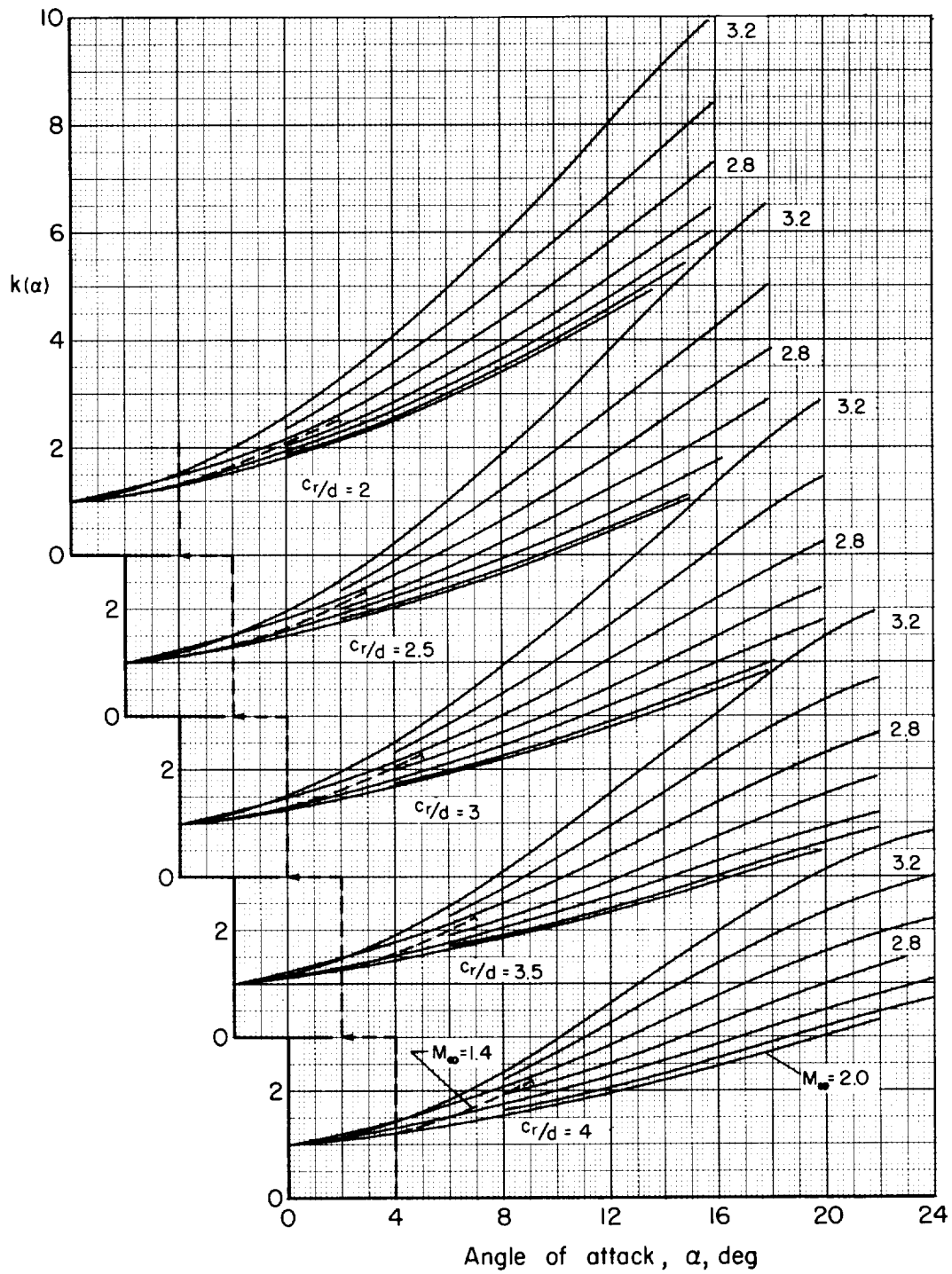
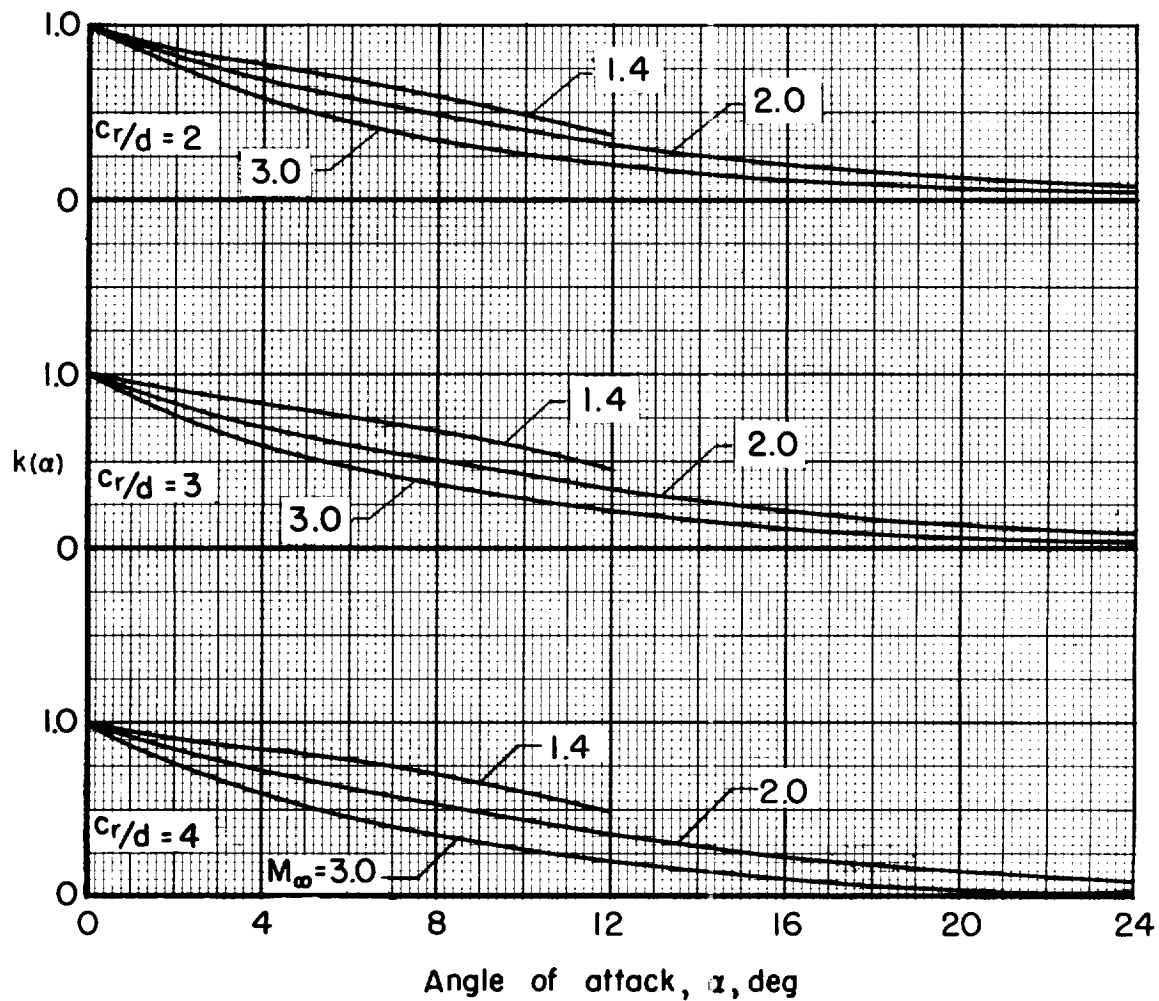


Figure 13.- Center-of-pressure location, \bar{c} , of wing-induced side force on body in terms of wing-root chords from juncture of wing leading edge and root chord, $\alpha = 0^\circ$.



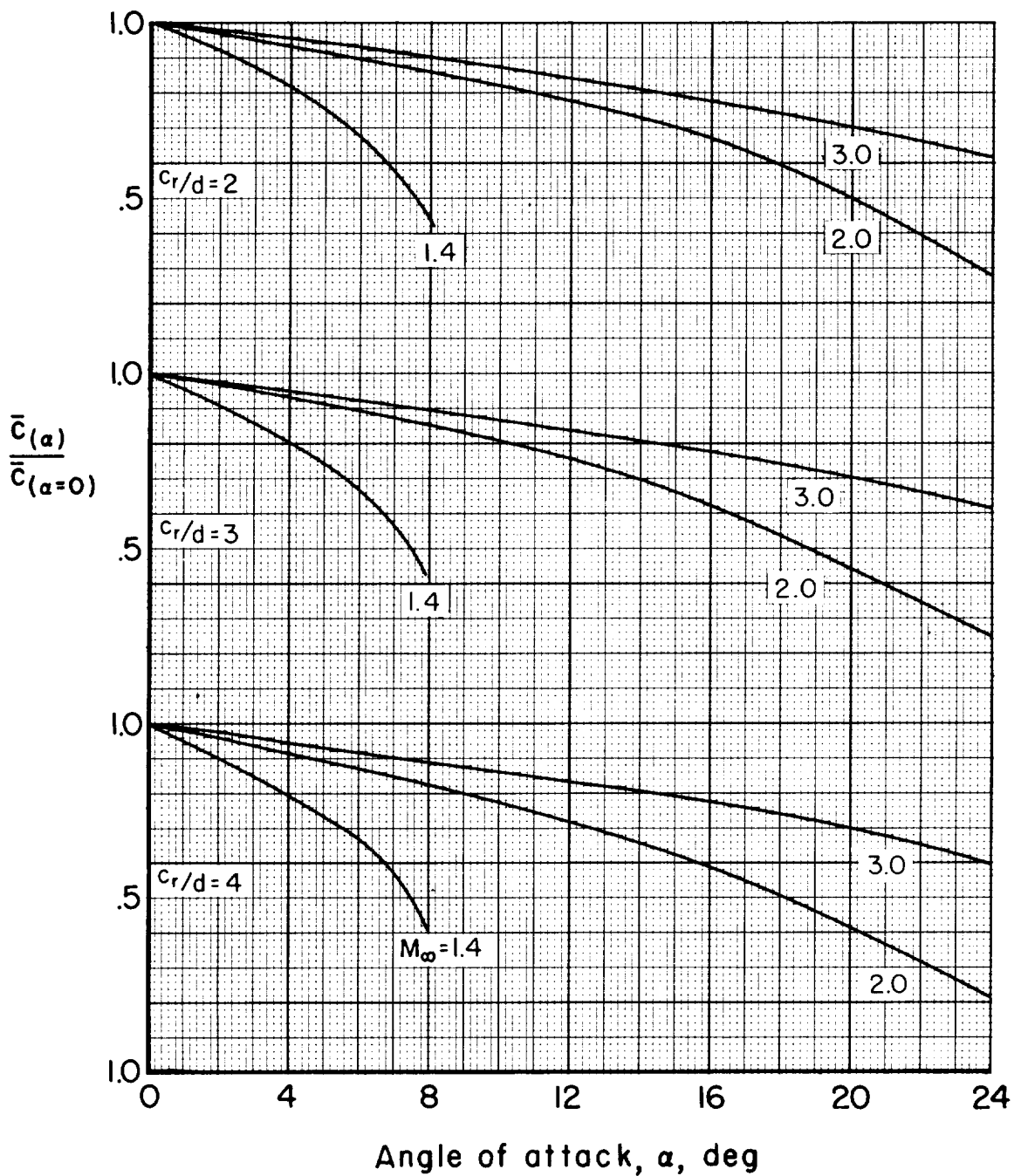
(a) High wing location.

Figure 14.- Interference coefficient $k(\alpha)$ as a function of angle of attack for various Mach numbers.



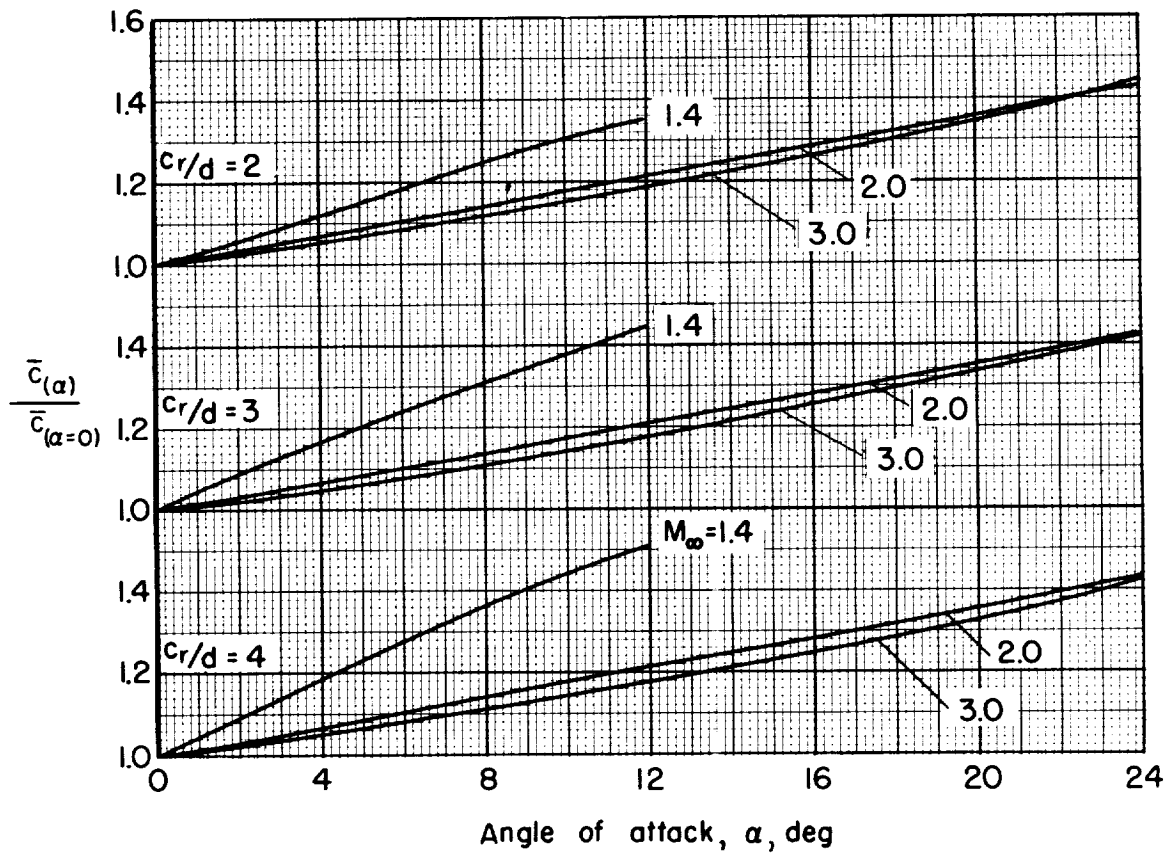
(b) Low wing location.

Figure 14.- Concluded.



(a) High wing location.

Figure 15.- Center-of-pressure location $\bar{c}(\alpha)$ of wing-induced side force on body in terms of $\bar{c}(\alpha=0)$.



(b) Low wing location.

Figure 15.- Concluded.

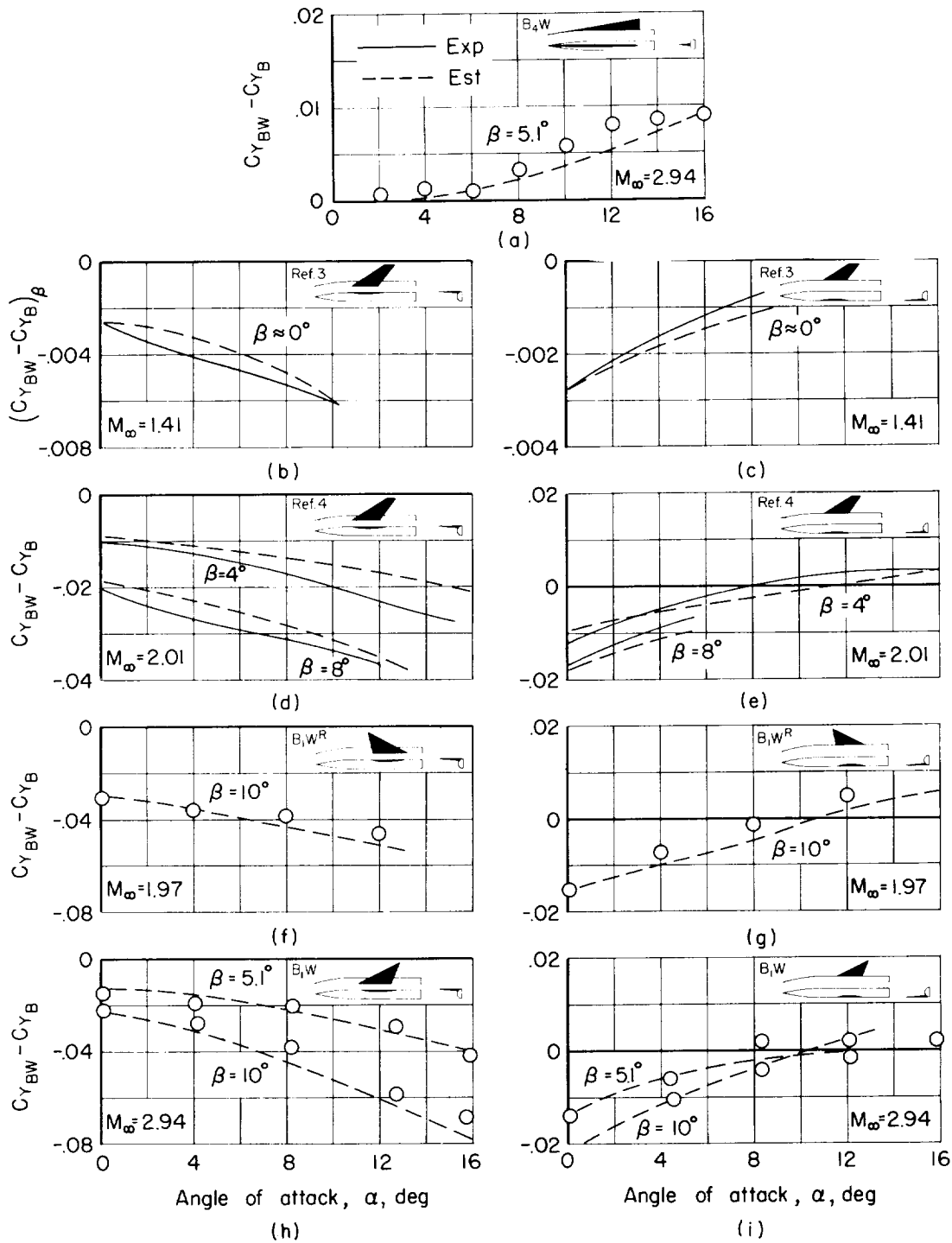


Figure 16.- Comparison of experimental and estimated side-force coefficient increments due to adding wing to body.

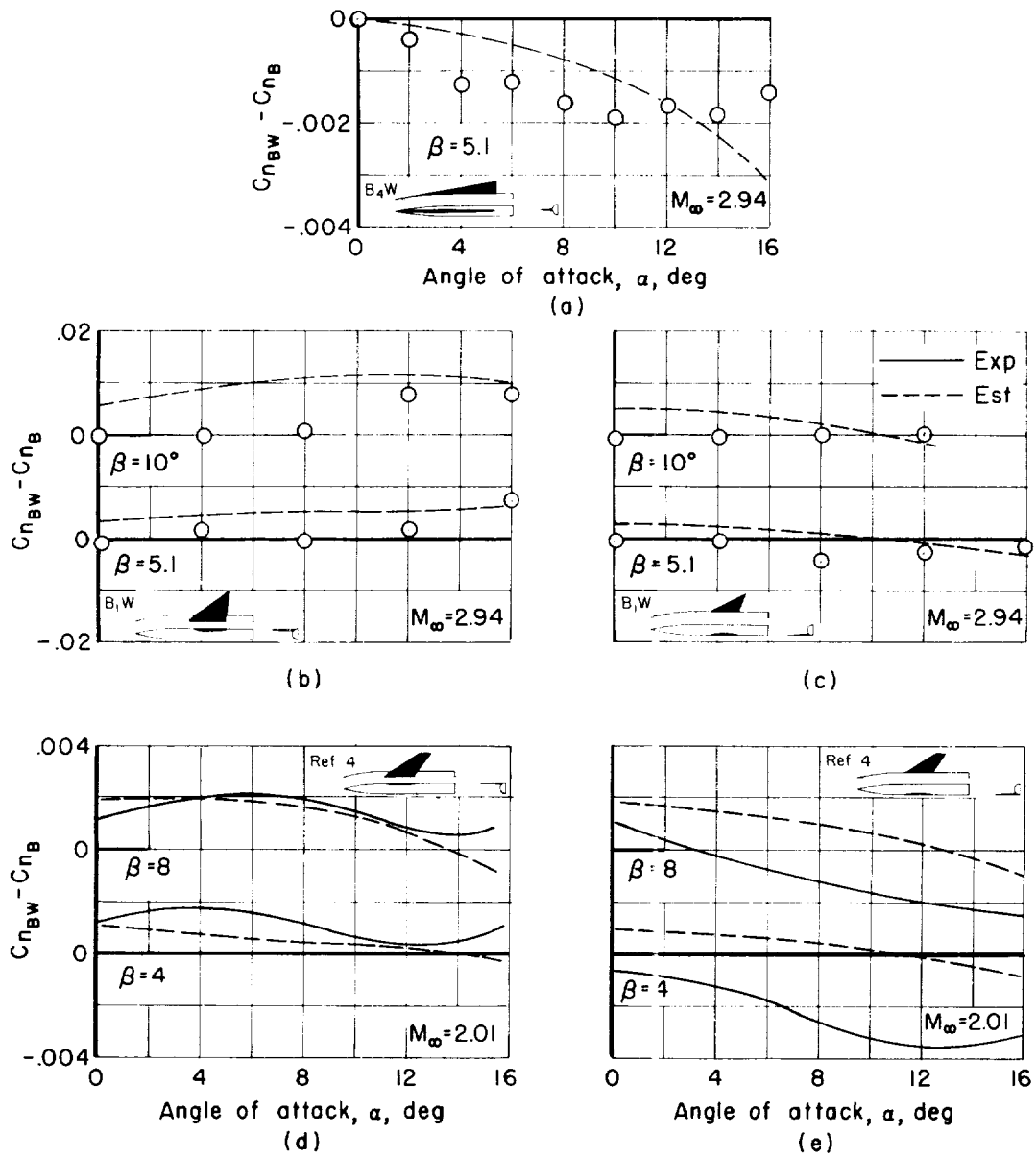
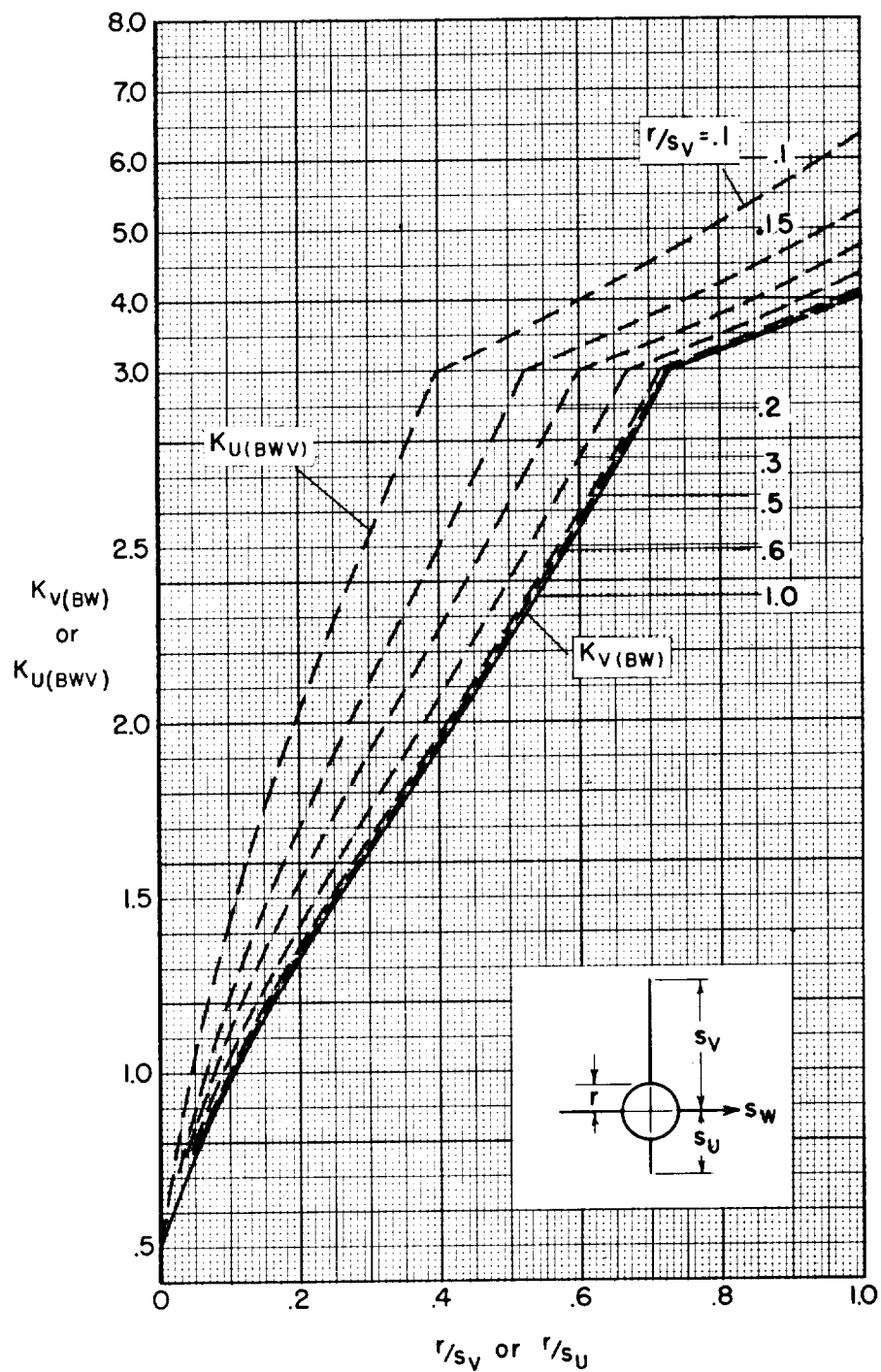
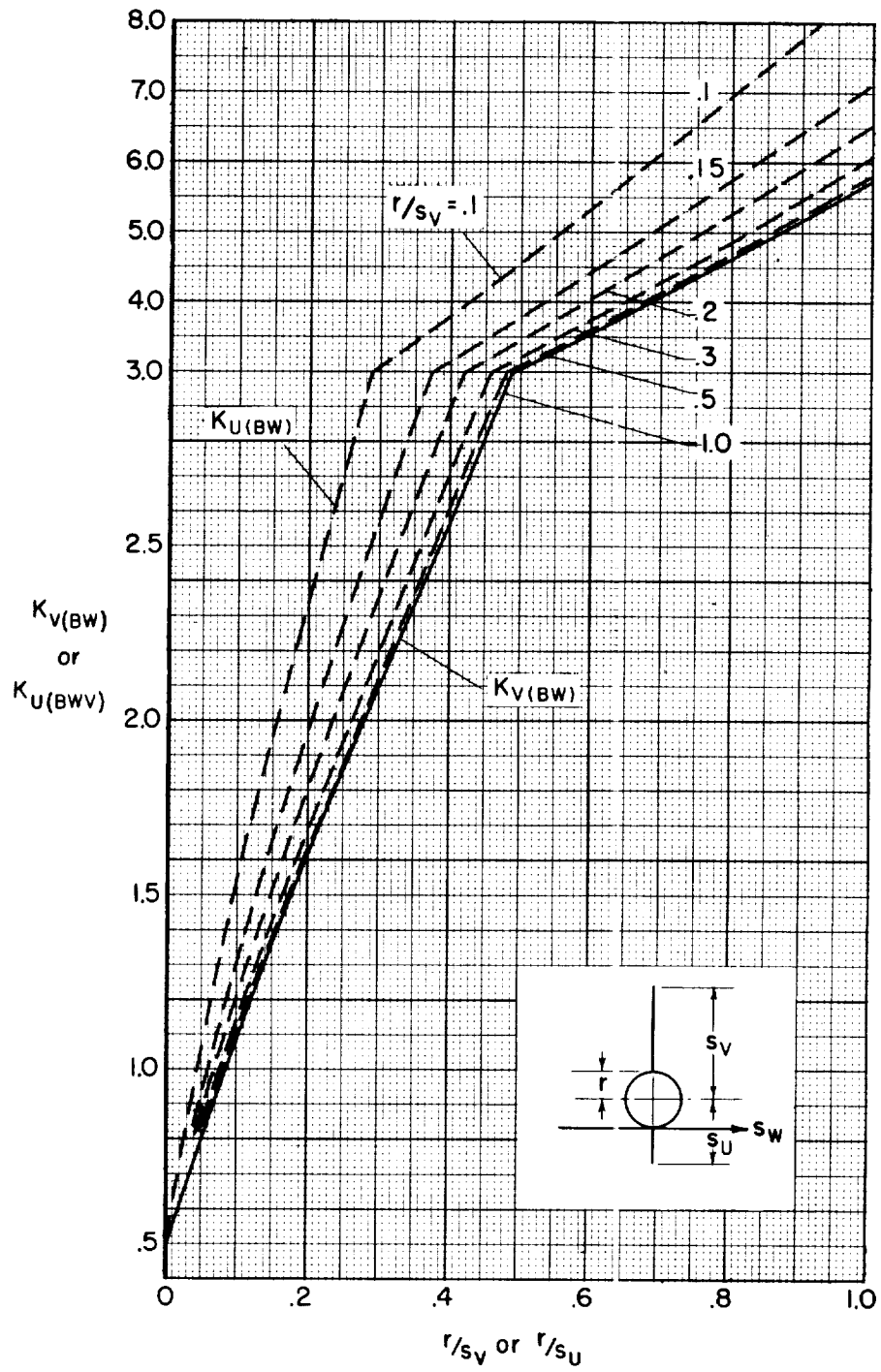


Figure 17.- Comparison of experimental and estimated yawing-moment coefficient increments due to adding wing to body.



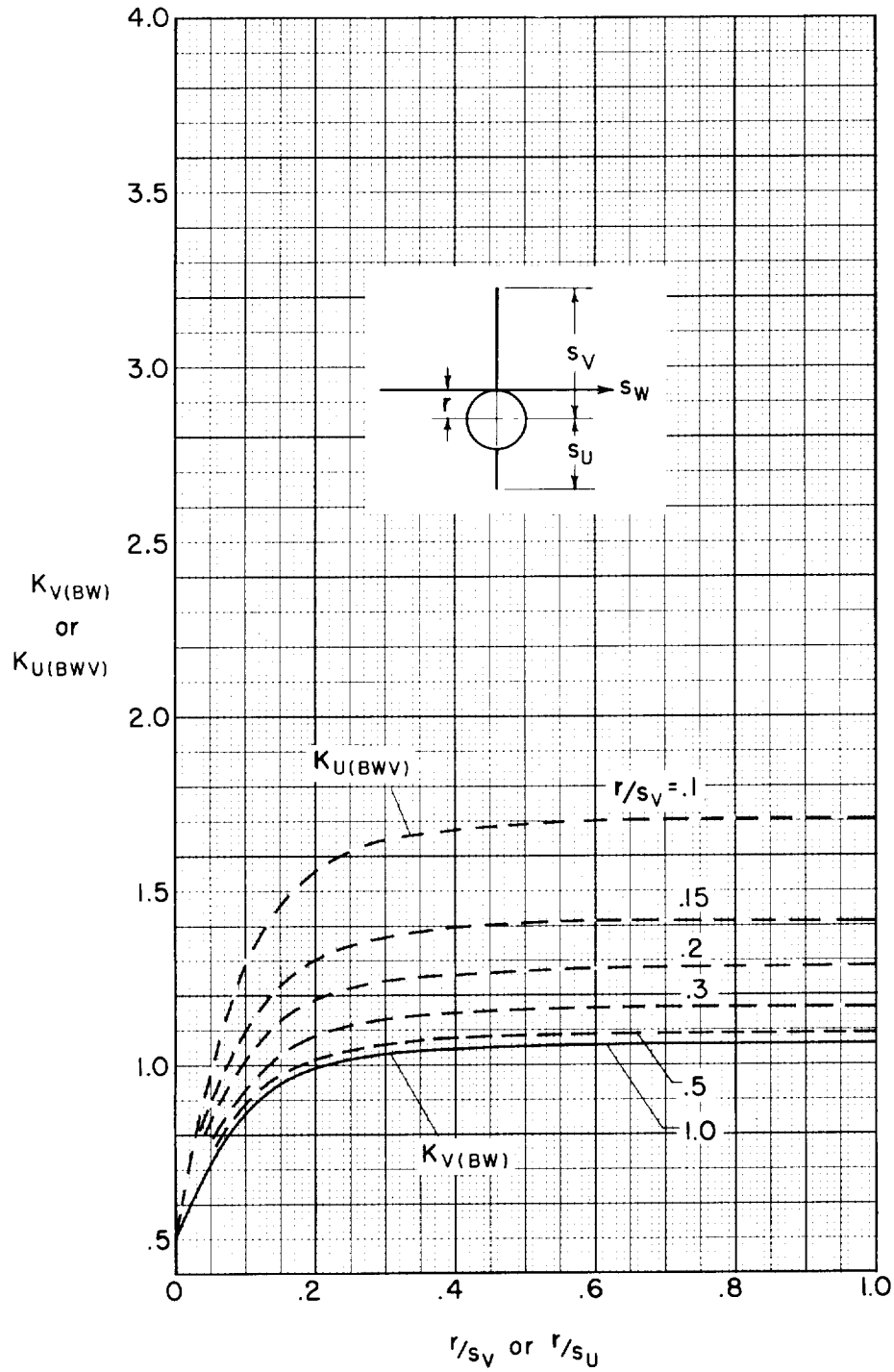
(a) Mid-wing location.

Figure 18.- Interference coefficients K for tails in presence of an $r/s_W = 0.2$ body-wing combination.



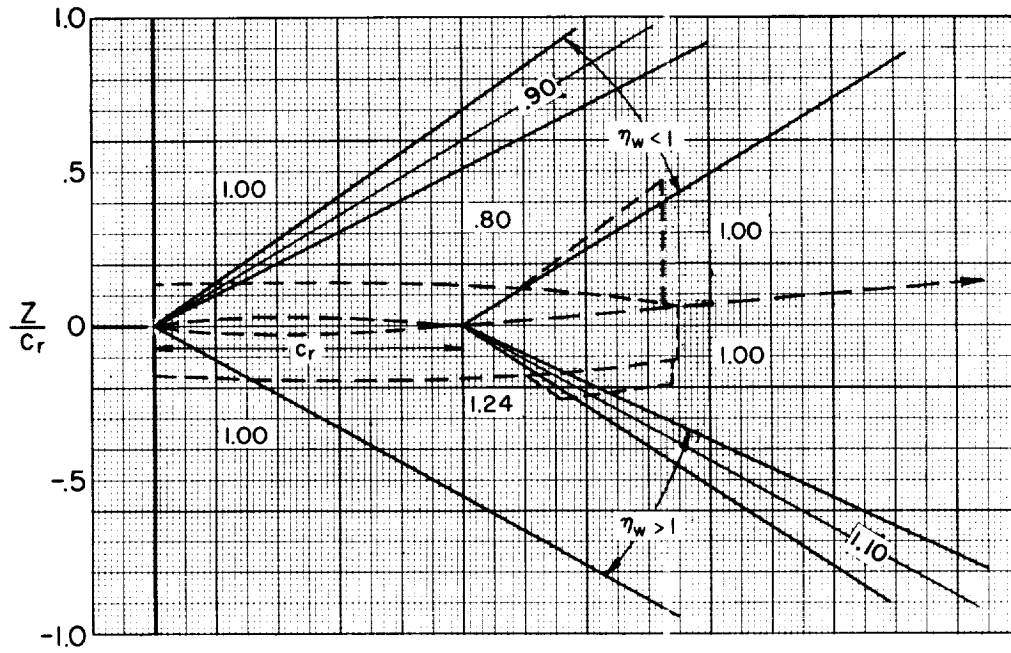
(b) Low wing location.

Figure 18.- Continued.

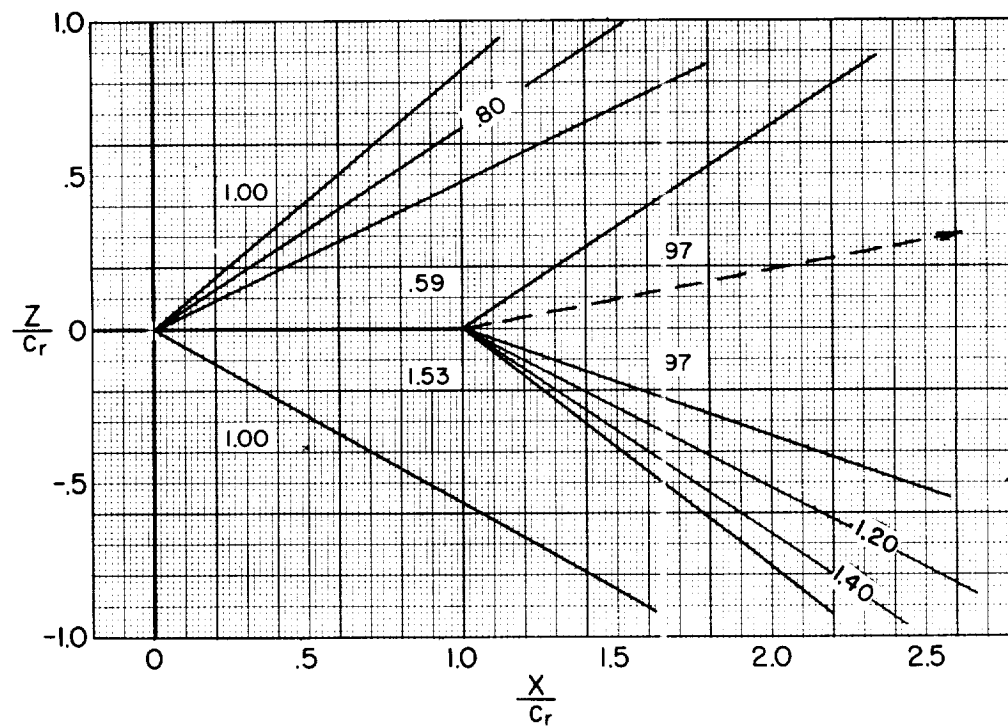


(c) High wing location.

Figure 18.- Concluded.



(a) $\alpha = 5^\circ, M_\infty = 2$



(b) $\alpha = 10^\circ, M_\infty = 2$

Figure 19.- Charts of tail effectiveness parameter η_w .

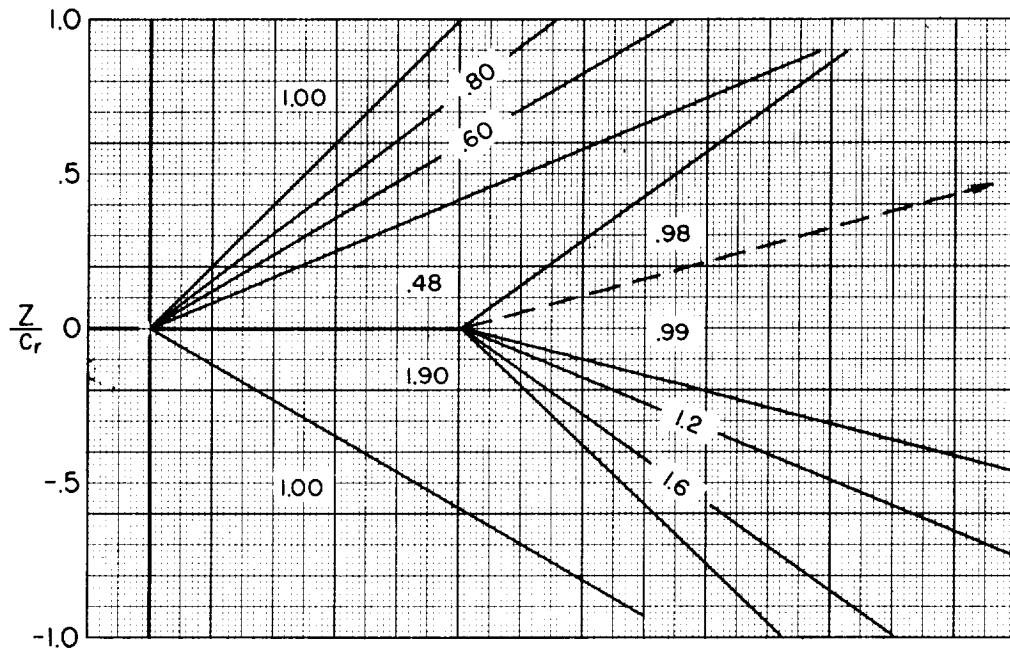
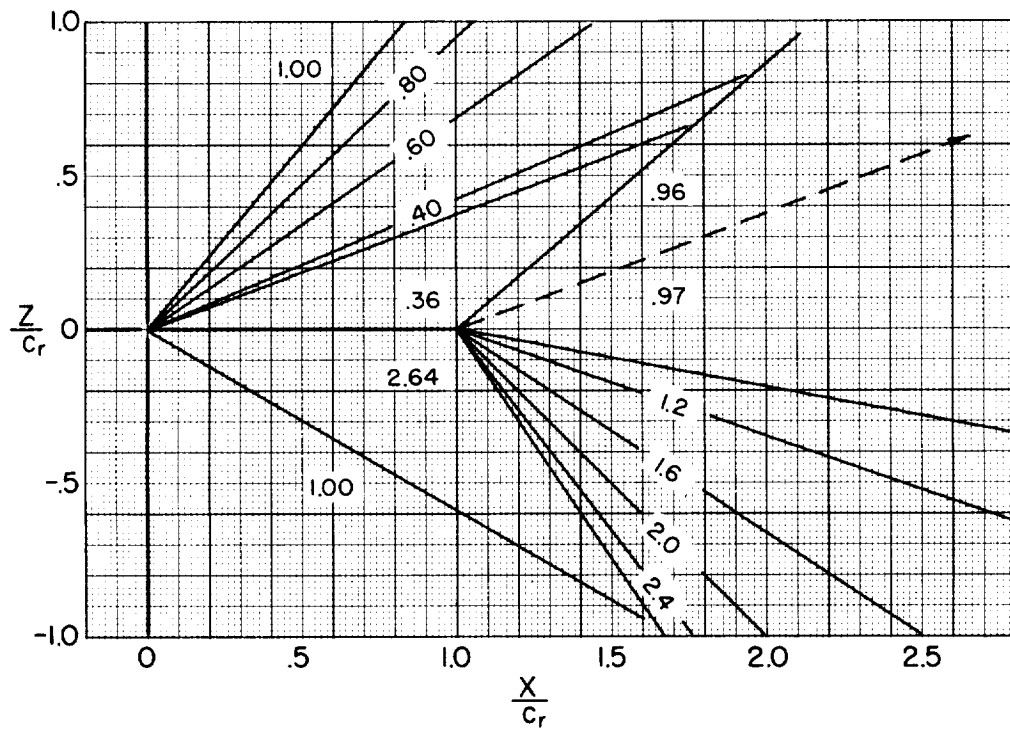
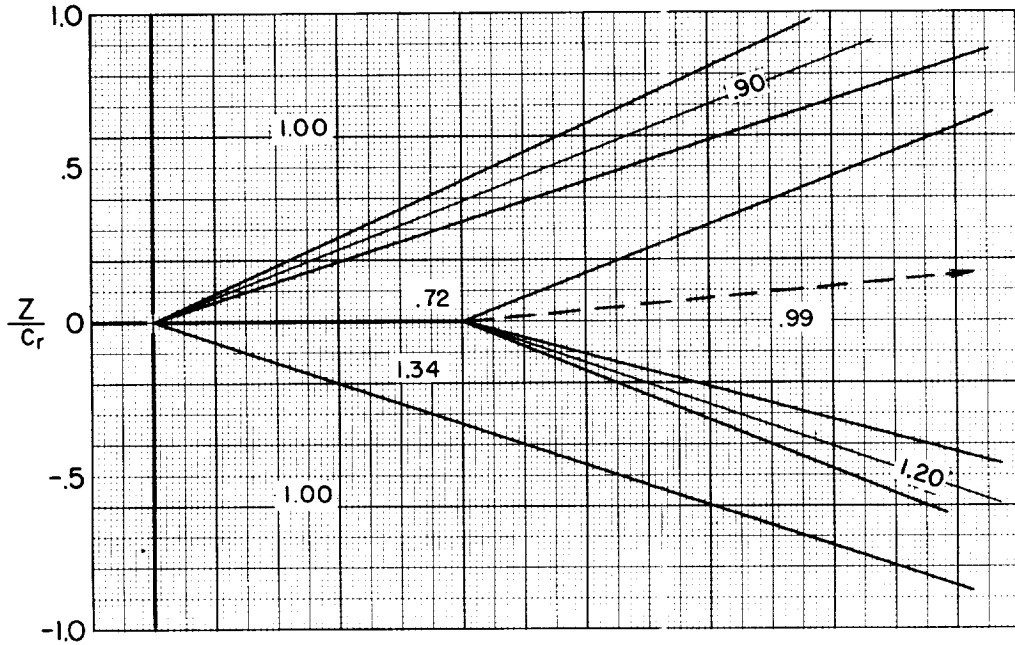
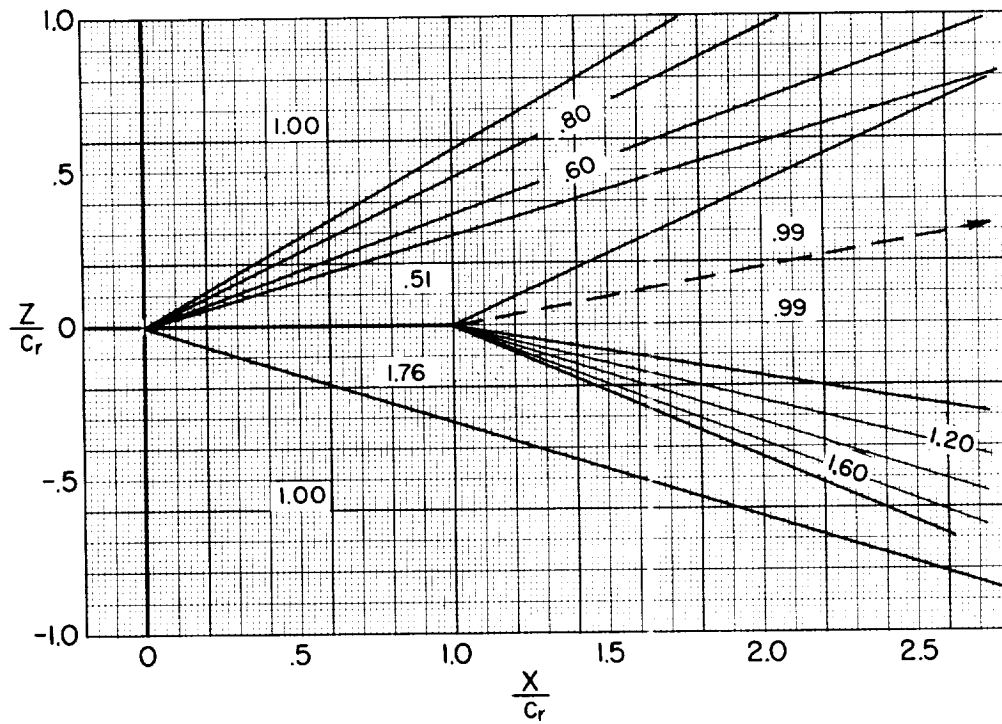
(c) $\alpha = 15^\circ$, $M_\infty = 2$ (d) $\alpha = 20^\circ$, $M_\infty = 2$

Figure 19.- Continued.



(e) $\alpha = 5^\circ, M_\infty = 3$



(f) $\alpha = 10^\circ, M_\infty = 3$

Figure 19.- Continued.

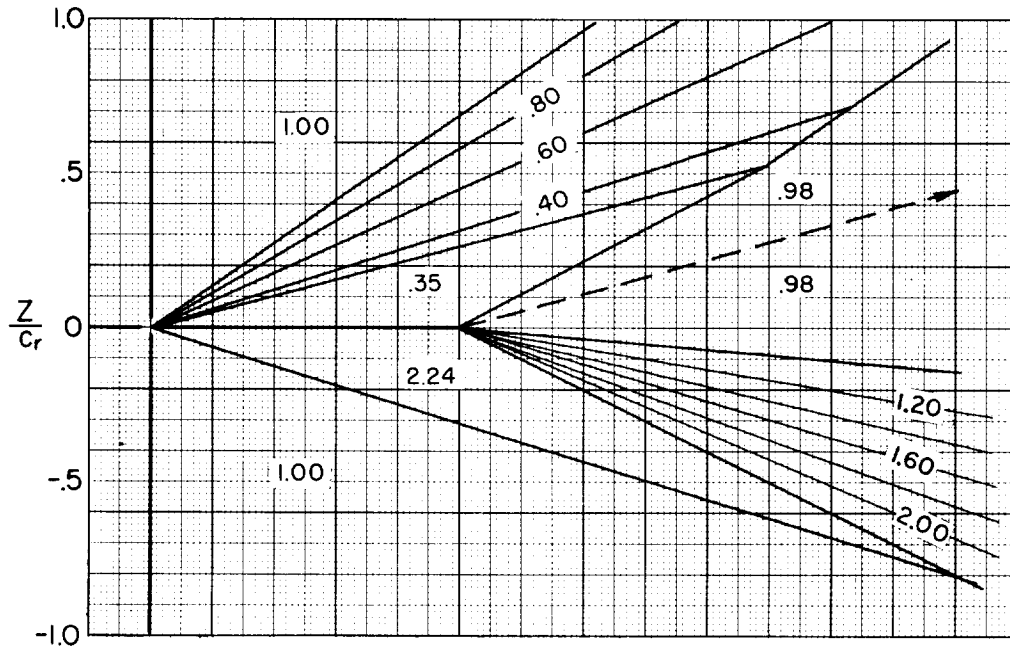
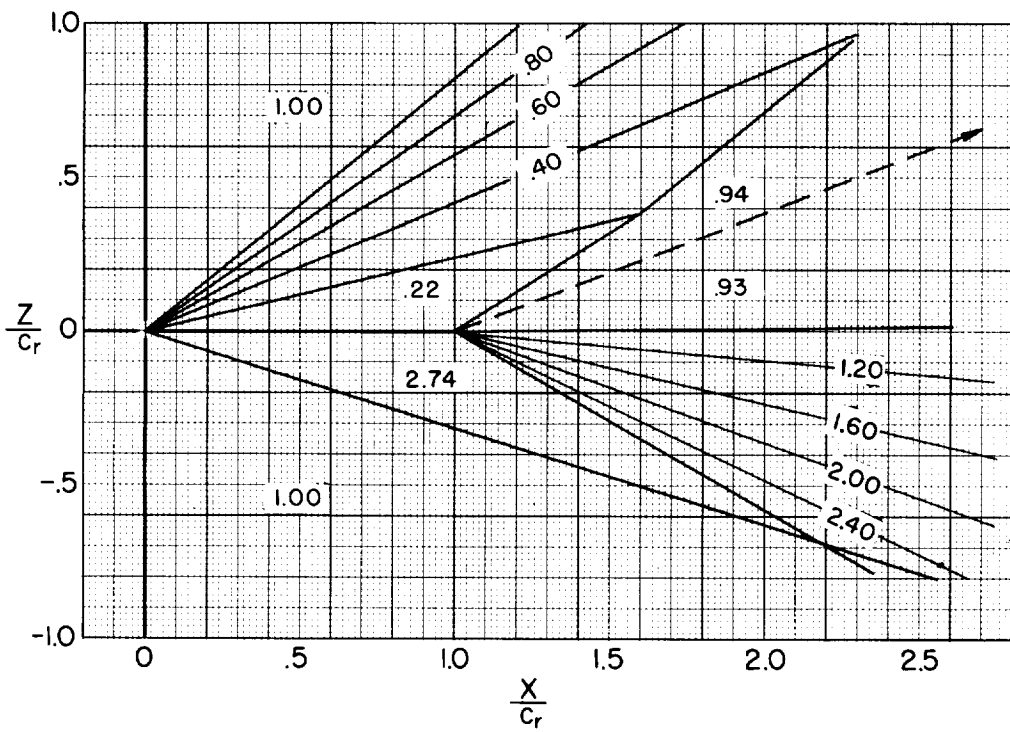
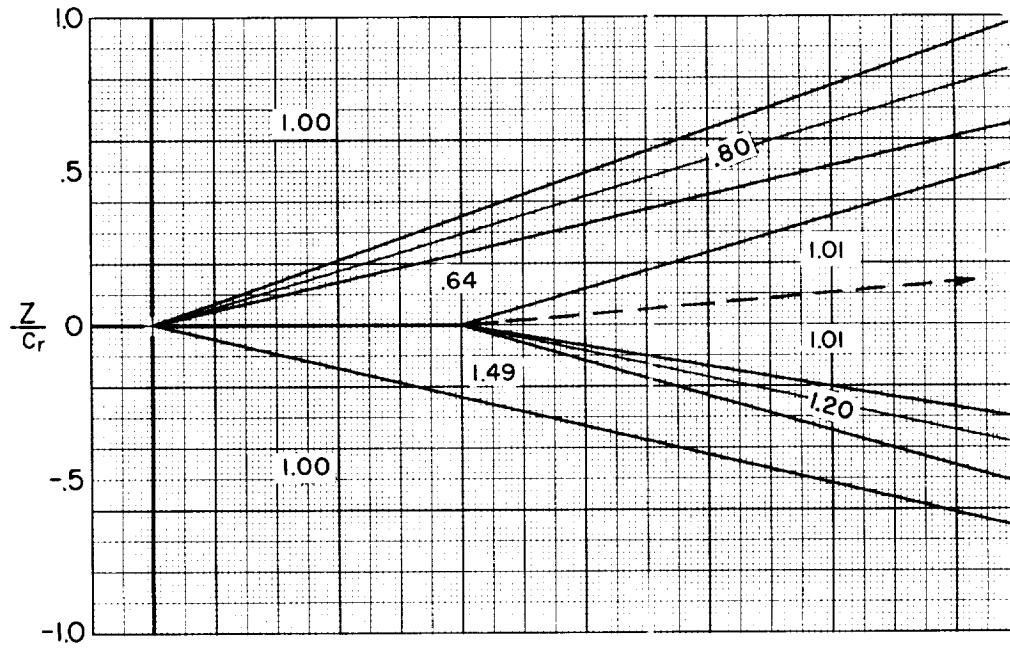
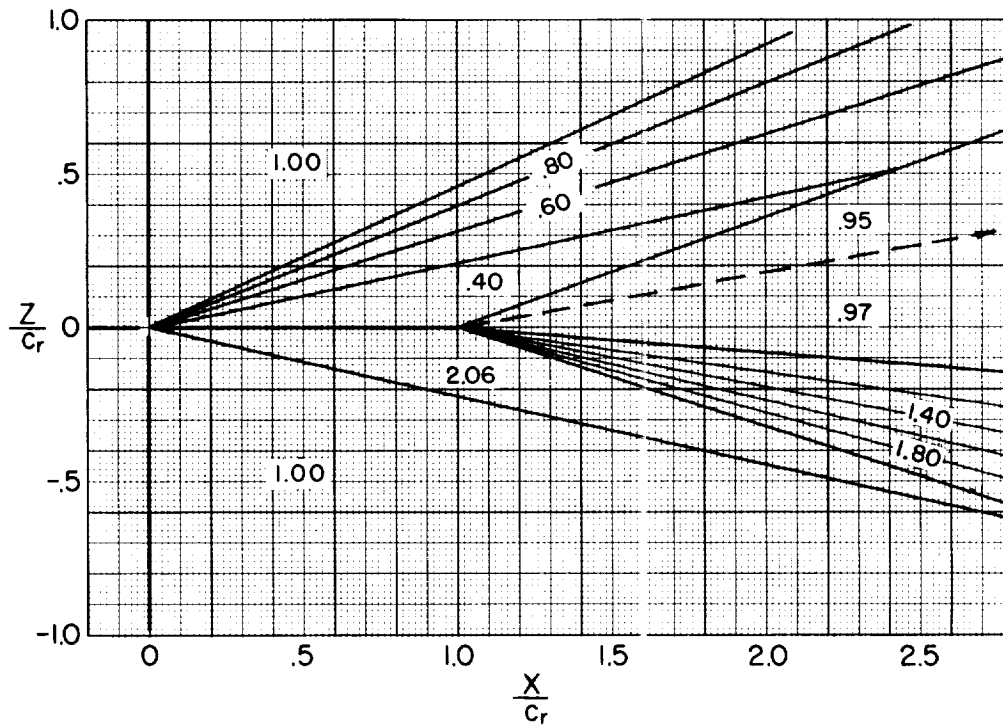
(g) $\alpha = 15^\circ$, $M_\infty = 3$ (h) $\alpha = 20^\circ$, $M_\infty = 3$

Figure 19.- Continued.



(i) $\alpha = 5^\circ$, $M_\infty = 4$



(j) $\alpha = 10^\circ$, $M_\infty = 4$

Figure 19.- Continued.

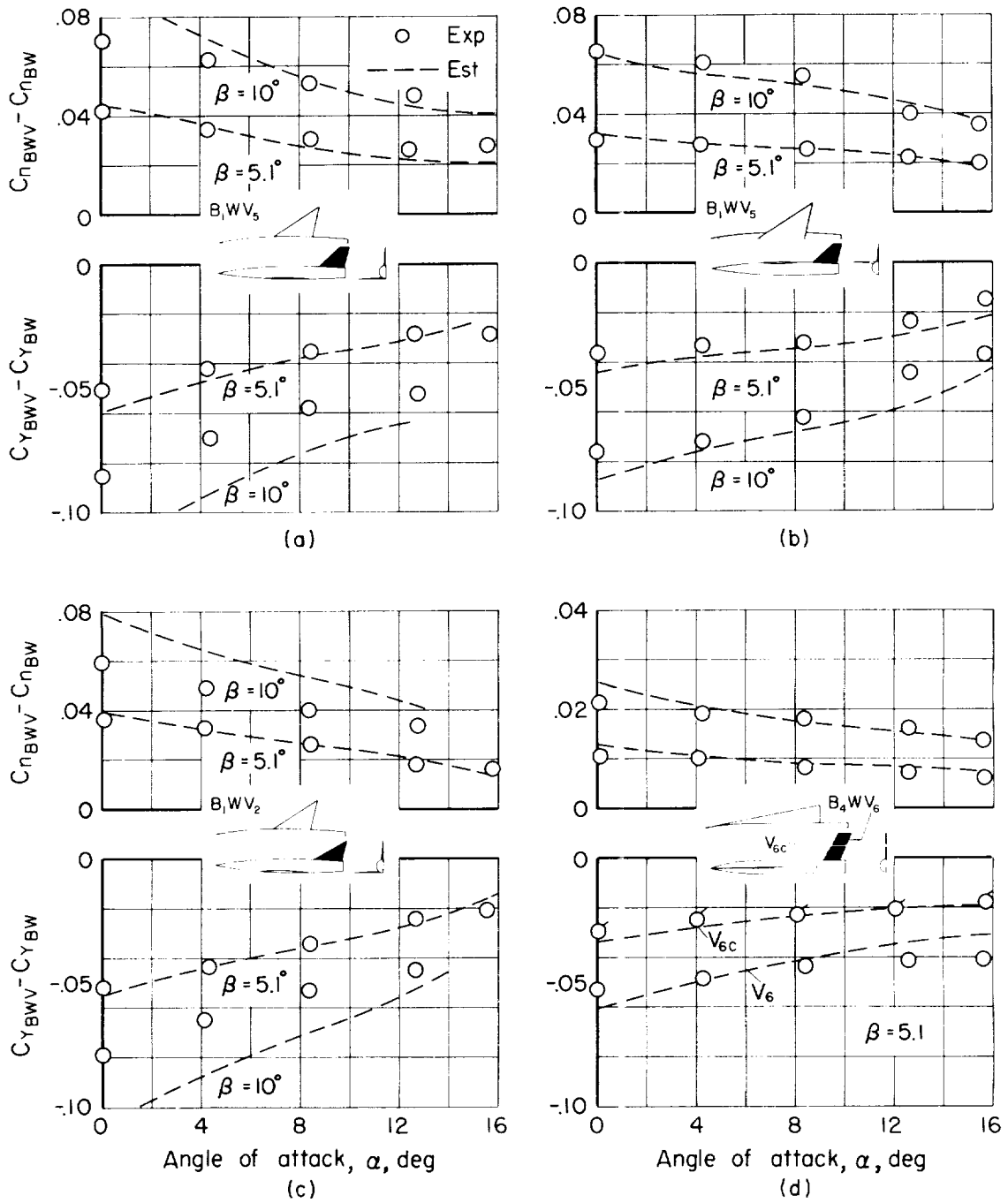


Figure 20.- Comparison of experimental and estimated side-force and yawing-moment coefficient increments resulting from addition of vertical tail to various body-wing combinations at $M_{\infty} = 2.94$.

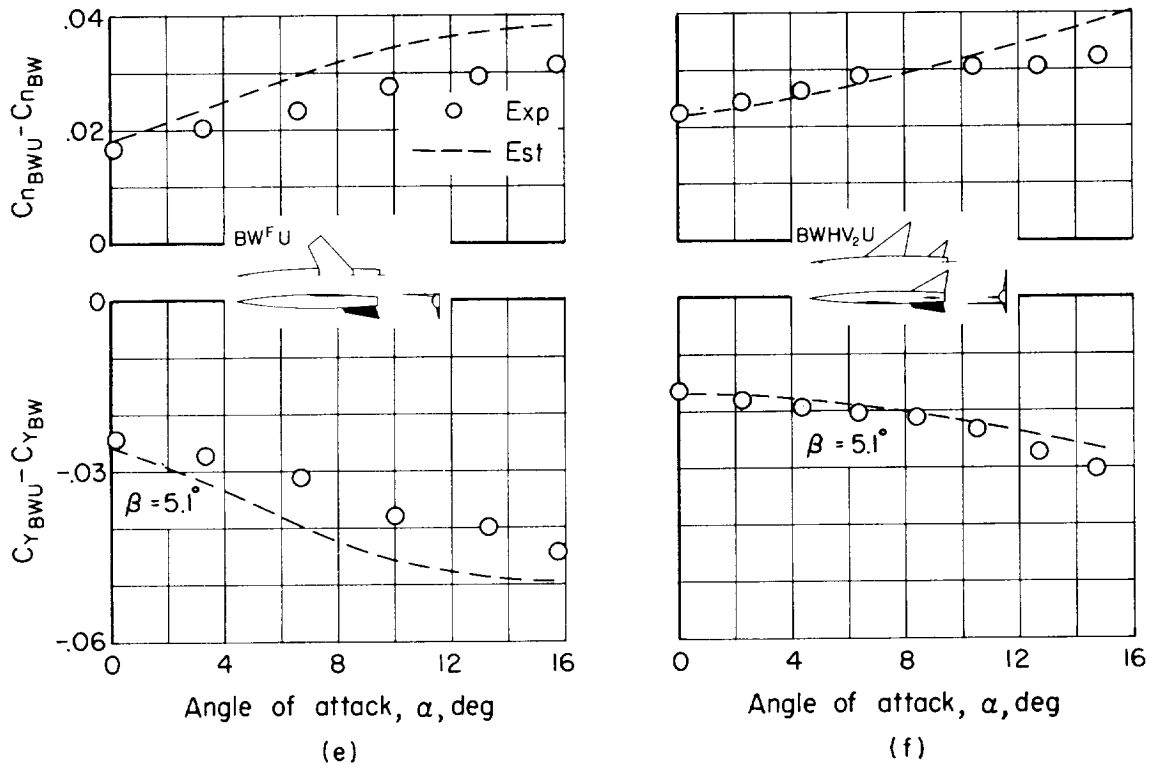


Figure 20.- Concluded.

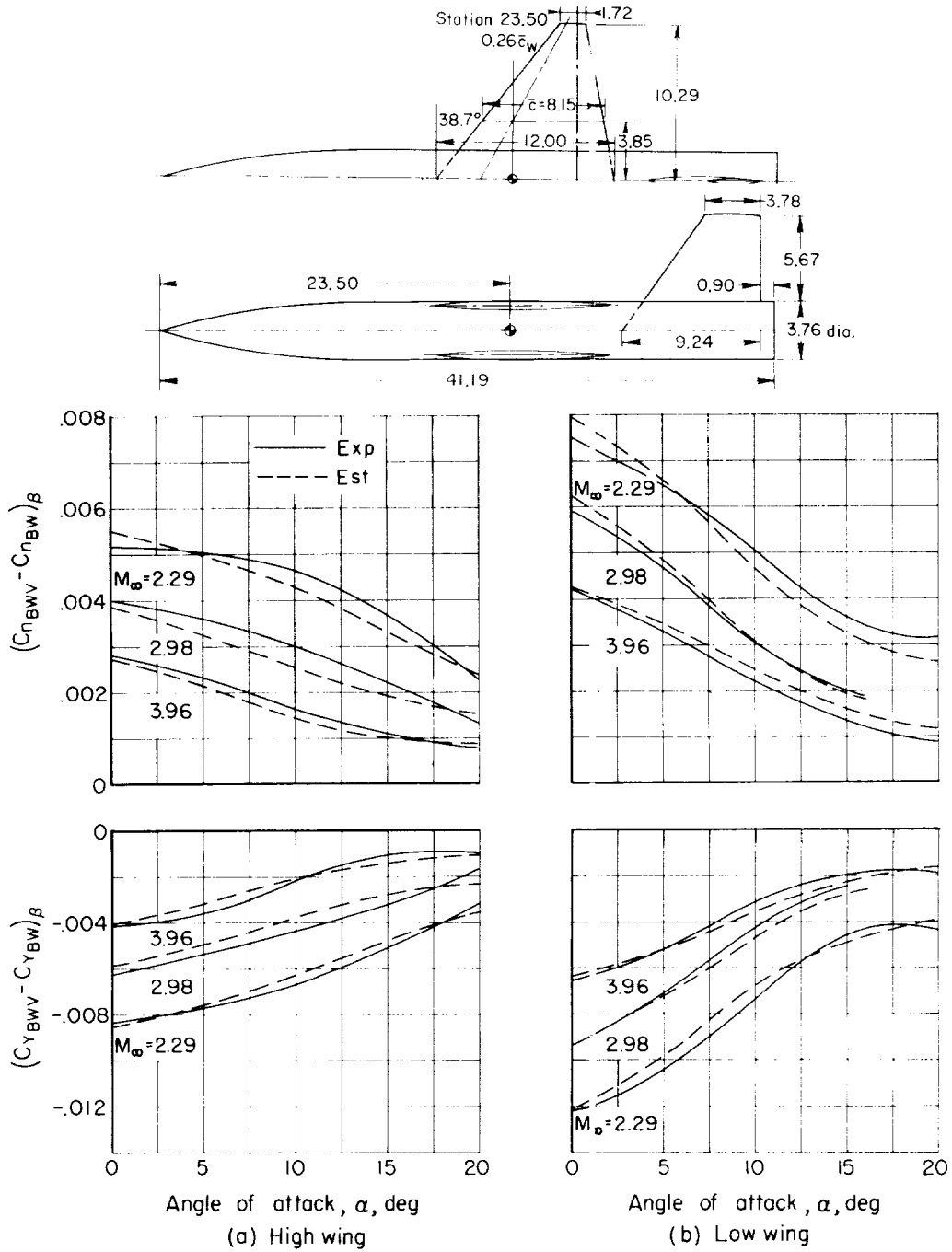


Figure 21.- Comparison of experimental and estimated side-force and yawing-moment coefficients resulting from addition of vertical tail to a body at various Mach numbers; unpublished data from tests in the Langley Unitary Plan wind tunnel.

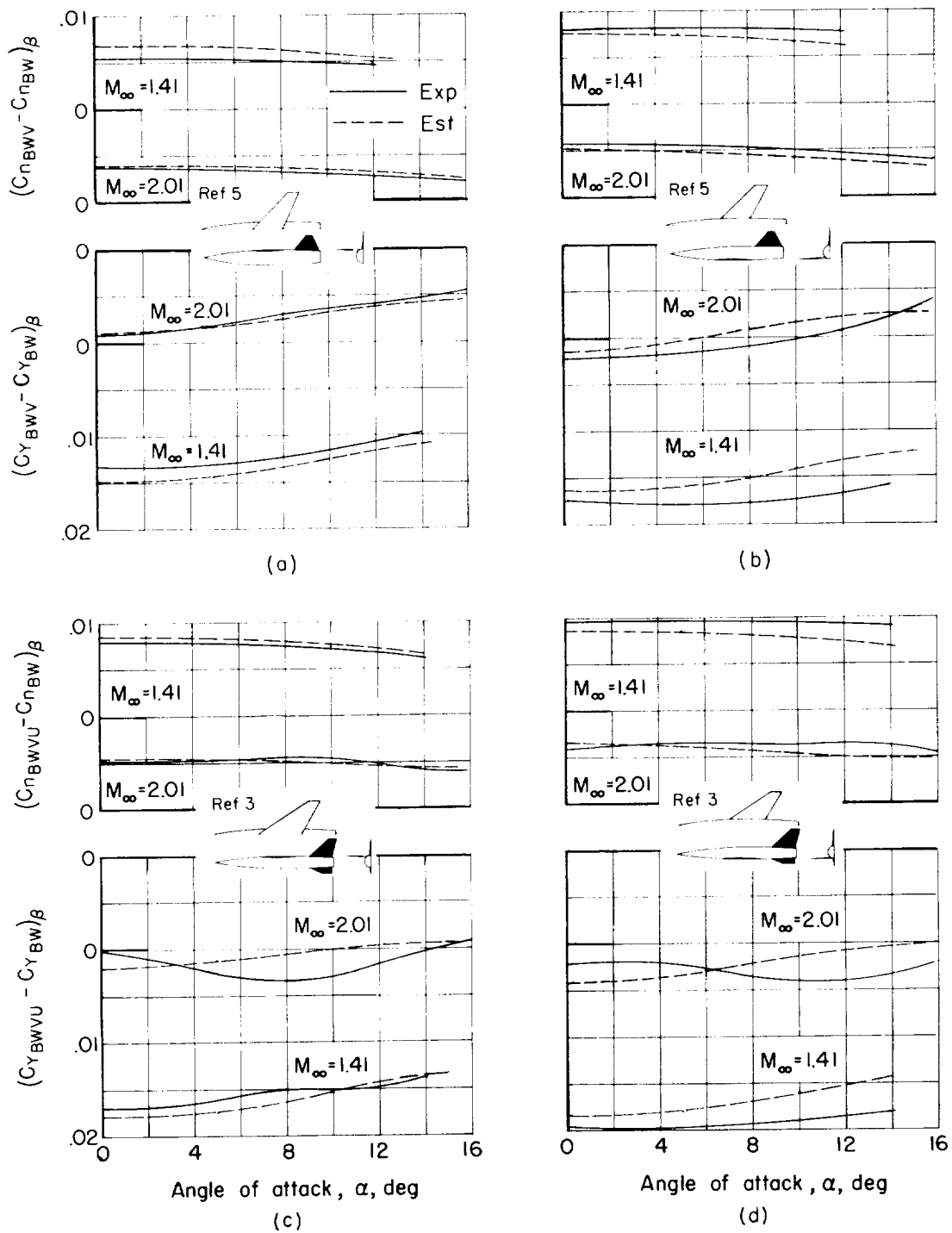


Figure 22.- Comparison of experimental and estimated side-force and yawing-moment coefficient increments resulting from addition of vertical tails to body-wing combinations at $M_\infty = 1.41$ and 2.01 .

